*Materials Science and Engineering R 52 (2006) 49–91*

**R Reports: A Review Journal**

www.elsevier.com/locate/mser

Available online at www.sciencedirect.com

SCIENCE DIRECT®

# Quasi-one-dimensional metal oxide materials—Synthesis, properties and applications

Jia Grace Lu*, Paichun Chang, Zhiyong Fan

*Department of Chemical Engineering and Materials Science & Department of Electrical Engineering and Computer Science, University of California-Irvine, Irvine, CA 92697, United States*

Available online 23 May 2006

## Abstract

Recent advances in the field of nanotechnology have led to the synthesis and characterization of an assortment of quasi-one-dimensional (Q1D) structures, such as nanowires, nanoneedles, nanobelts and nanotubes. These fascinating materials exhibit novel physical properties owing to their unique geometry with high aspect ratio. They are the potential building blocks for a wide range of nanoscale electronics, optoelectronics, magnetoelectronics, and sensing devices. Many techniques have been developed to grow these nanostructures with various compositions. Parallel to the success with group IV and groups III–V compounds semiconductor nanostructures, semiconducting metal oxide materials with typically wide band gaps are attracting increasing attention.

This article provides a comprehensive review of the state-of-the-art research activities that focus on the Q1D metal oxide systems and their physical property characterizations. It begins with the synthetic mechanisms and methods that have been exploited to form these structures. A range of remarkable characteristics are then presented, organized into sections covering a number of metal oxides, such as ZnO, $In_2O_3$, $SnO_2$, $Ga_2O_3$, and $TiO_2$, etc., describing their electrical, optical, magnetic, mechanical and chemical sensing properties. These studies constitute the basis for developing versatile applications based on metal oxide Q1D systems, and the current progress in device development will be highlighted.



*Keywords:* Metal oxide semiconductor; Quasi-one-dimensional system; Nanoelectronics; Field-effect transistor; Light-emitting diode; Chemical sensor

## 1. Introduction

In the present development of microelectronics, Moore's law [1] continues to dominate as the number of transistors per chip doubles every 2 years. Soon the microprocessor architecture will reach over a billion transistors per chip operating at clock rates exceeding 10 GHz. Such device miniaturization trend will not only be hindered by the current fabrication technology, but also result in dramatically increased power consumption. In addition, the projected channel length of 20 nm in CMOS field-effect transistor by the year 2014 will decrease the gate oxide thickness to about two monolayers [2]. Consequently, the associated tunneling-induced leakage current and dielectric breakdown will lead to device failure.

As one of the national initiative, nanotechnology, which exploits materials of dimension smaller than 100 nm, is addressing the challenge and offering exciting new possibilities. This is in accord with Richard Feynman's speech back in 1959, when he described a vision – "to synthesize nanoscale

* Corresponding author. Tel.: +1 949 824 8714; fax: +1 949 824 4040.
*E-mail address:* jglu@uci.edu (J.G. Lu).

0927-796X/$ – see front matter 
doi:10.1016/j.mser.2006.04.002

building blocks with precisely controlled size and composition, and assemble them into larger structures with unique properties and functions'' [3]. This vision has sparked the imagination of a generation of researchers.

One class of nanoscale materials which has attracted tremendous attention is the quasi-one-dimensional (Q1D) system since the revolutionary discovery of carbon nanotubes in 1991. Enormous progress has been achieved in the synthesis, characterization, and device application of the Q1D systems. These structures with high aspect ratio (i.e., size confinement in two coordinates) offer better crystallinity, higher integration density, and lower power consumption. And due to a large surface-to-volume ratio and a Debye length comparable to the small size, they demonstrate superior sensitivity to surface chemical processes. In addition, their size confinement renders tunable band gap, higher optical gain and faster operation speed.

A variety of inorganic nanomaterials, including single element and compound semiconductors, have been successfully synthesized [4]. With their in-depth physical property characterizations, they have demonstrated to be promising candidates for future nanoscale electronic, optoelectronic and sensing device applications. Among the semiconductors, metal oxides stand out as one of the most versatile materials, owing to their diverse properties and functionalities. Their Q1D structures not only inherit the fascinating properties from their bulk form such as piezoelectricity, chemical sensing, and photodetection, but also possess unique properties associated with their highly anisotropic geometry and size confinement.

This article will provide a comprehensive review of the state-of-the-art research activities that focus on the synthetic strategies, physical property characterizations and device applications of these Q1D metal oxides. This review is divided into three main sections. The first section introduces the bottom-up assembly methods employed in synthesizing Q1D metal oxides. The approaches are classified into vapor phase growth and liquid phase growth. This section also discusses the underlying growth mechanisms for the rational synthesis of the Q1D metal oxides, and describes the control of size, growth position, alignment, substrate lattice matching, and doping. Next, a range of remarkable electrical, optical and chemical sensing characteristics are presented in the second section, organized into sub-sections based on some representative metal oxide materials, such as ZnO, $In_2O_3$, $Ga_2O_3$, $SnO_2$, $Fe_2O_3$, $Fe_3O_4$, CuO, CdO, $TiO_2$ and $V_2O_5$. Based on these fundamental physical properties, the recent progress of Q1D functional elements and their integration into electronic devices will be highlighted in the third section. This includes field-effect transistor, logic gates, light emission diode, photodetector, photovoltaic device, chemical sensor, field emitter, mechanical resonator, etc. The article will conclude with a prospective outlook of some scientific and technological challenges that remain for further investigation in this field.

## 2. Synthesis and construction of metal oxide Q1D systems

A variety of methods have been utilized to grow Q1D nanostructures. According to the synthesis environment, they can be mainly divided into two categories: vapor phase growth and liquid (solution) phase growth. Most of the metal oxide nanostructures are grown via the well-developed vapor phase technique, which is based on the reaction between metal vapor and oxygen gas. The governing mechanisms are the vapor–liquid–solid process (VLS) and vapor–solid process (VS). On the other hand, solution-phase growth methods provide more flexible synthesis process and an alternative to achieve lower cost. This section will present a survey of various reports on the synthesis of Q1D metal oxides using these methods.

## 2.1. Material growth

### 2.1.1. Vapor phase growth

High-temperature vapor phase growth assisted by a thermal furnace is a straightforward approach that controls the reaction between metal vapor source and oxygen gas. In order to control the diameter, aspect ratio, and crystallinity, diverse techniques have been exploited including thermal chemical vapor deposition (CVD), direct thermal evaporation [5], pulse-laser-deposition (PLD) [6–8], and metal–organic chemical vapor deposition (MOCVD) [9–11], etc. These growth methods are based on two mechanisms: vapor–liquid–solid and vapor–solid.

*2.1.1.1. Vapor–liquid–solid mechanism.* VLS mechanism was first proposed by Wagner and Ellis in 1964 [12] while observing the growth of Si whisker [13]. In essence, VLS is a catalyst-assisted growth process which uses metal nanoclusters or nanoparticles as the nucleation seeds. These nucleation seeds determine the interfacial energy, growth direction and diameter of Q1D nanostructure. Therefore, proper choice of catalyst is critical. In the case of growing Q1D metal oxides, VLS process is initiated by the formation of liquid alloy droplet which contains both catalyst and source metal. Precipitation occurs when the liquid droplet becomes supersaturated with the source metal. Under the flow of oxygen, Q1D metal oxide crystal is formed [14]. Normally the resulting crystal is grown along one particular crystallographic orientation which corresponds to the minimum atomic stacking energy, leading to Q1D structure formation. This type of growth is epitaxial, thus it results in high crystalline quality. Wu et al. have provided direct evidence of VLS growth by means of real time in situ transmission electron microscope observations [15]. This work depicts a vivid dynamic insight and elucidates the understanding of such microscopic chemical process.

A majority of oxide nanowires has been synthesized via this catalyst-assisted mechanism, such as ZnO [16], MgO [17], CdO [8], $TiO_2$ [18], $SnO_2$ [19], $In_2O_3$ [20], and $Ga_2O_3$ [21]. Several approaches have been developed based on the VLS mechanism. As an example, thermal CVD synthesis process utilizes a thermal furnace to vaporize the metal source, then proper amount of oxygen gas is introduced through mass flow controller. In fact, metal and oxygen vapor can be supplied via different ways, such as carbothermal or hydrogen reduction of metal oxide source material [22,23] and flowing water vapor instead of oxygen [24,25]. Fig. 1 shows a typical thermal CVD set up consisting of a horizontal quartz tube and a resistive heating furnace. Source material is placed inside the quartz tube; another substrate ($SiO_2$, sapphire, etc.) deposited with catalyst nanoparticles is placed at downstream for nanostructure growth.

*2.1.1.2. Vapor–solid mechanism.* VS process occurs in many catalyst-free growth processes [26–29]. It is a commonly observed phenomenon but still lacks fundamental understanding. Quite a few

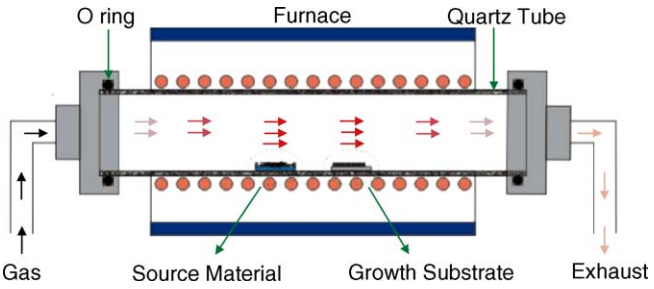


Fig. 1. A schematic of a thermal furnace synthesis system that is used in vapor phase growth methods including CVD, thermal evaporation, and PLD.

experimental and theoretical works have proposed that the minimization of surface free energy primarily governs the VS process [30–32]. Under high temperature condition, source materials are vaporized and then directly condensed on the substrate placed in the low temperature region. Once the condensation process happens, the initially condensed molecules form seed crystals serving as the nucleation sites. As a result, they facilitate directional growth to minimize the surface energy. This self-catalytic growth associated with many thermodynamic parameters is a rather complicated process that needs quantitative modeling.

*2.1.2. Solution-phase growth*

Growth of nanowires, nanorods and nanoneedles in solution phase has been successfully achieved. This growth method usually requires ambient temperature so that it considerably reduces the complexity and cost of fabrication. To develop strategies that can guide and confine the growth direction to form Q1D nanostructures, researchers have used a number of approaches which may be grouped into template-assisted method and template-free method.

*2.1.2.1. Template-assisted synthesis.* Large-area patterning of Q1D metal oxide nanowire array assisted by template has been achieved [33]. By utilizing periodic structured template, such as anodic aluminum oxide, molecular sieves, and polymer membranes, nanostructures can form inside the confined channels. For example, anodic aluminum oxide (AAO) membranes have embedded hexagonally ordered nanochannels. They are prepared via the anodization of pure aluminum in acidic solution [34]. These pores can be filled to form Q1D nanostructures using electrodeposition and sol–gel deposition methods. Because the diameter of these nanochannels and the inter-channel distance are easily controlled by the anodization voltage, it provides a convenient way to manipulate the aspect ratio and the area density of Q1D nanostructures.

*2.1.2.1.1. Electrochemical deposition.* Electrochemical deposition has been widely used to fabricate metallic nanowires in porous structures. It was found that it is also a convenient method to synthesize metal oxide nanostructures. In fact, there are both direct and indirect approaches to fabricate Q1D metal oxides using electrodeposition. In the direct method, by carefully choosing the electrolyte, ZnO [35], $Fe_2O_3$ [36], $Cu_2O$ [37] and NiO [38] Q1D structures have been successfully synthesized. In an indirect approach, Chen et al. [39] deposited tin metal into AAO and then thermally annealed it for 10 h to obtain $SnO_2$ nanowires embedded in the template. ZnO nanowires had also been obtained by this method [40].

*2.1.2.1.2. Sol–gel deposition.* In general, sol–gel process is associated with a gel composed of sol particles. As the first step, colloidal (sol) suspension of the desired particles is prepared from the solution of precursor molecules. An AAO template will be immersed into the sol suspension, so that the sol will aggregate on the AAO template surface. With an appropriate deposition time, sol particles can fill the channels and form structures with high aspect ratio. The final product will be obtained after a thermal treatment to remove the gel. Sol–gel method has been utilized to obtain ZnO [41] by soaking AAO into zinc nitrate solution mixed with urea and kept at 80 °C for 24–48 h followed by thermal heating. $MnO_2$ [42], $ZrO_2$ [43], $TiO_2$ [44], and various multi-compound oxide nanorods [45,46] had been synthesized based on similar processes.

*2.1.2.2. Template-free methods.* Instead of plating nanomaterials inside a template, much research effort is triggered to develop new techniques to direct Q1D nanostructure growth in liquid environment. Several methods will be described below including surfactant method, sonochemistry, and hydrothermal technique.

*2.1.2.2.1. Surfactant-assisted growth.* Surfactant-promoted anisotropic Q1D crystal growth has been considered as a convenient way to synthesize oxide nanowires. This anisotropic growth is often carried out in a microemulsion system composed of three phases: oil phase, surfactant phase and aqueous phase. In the emulsion system, these surfactants serve as microreactors to confine the crystal growth. To obtain desired materials, one needs to prudently select the species of precursor and surfactants, and also set the other parameters such as temperature, pH value, and concentration of the reactants. As a result, surfactant-assisted system is a trial-and-error based procedure which requires much endeavor to choose proper capping agents and reaction environment. By using this process, Xu et al. had synthesized ZnO [47], $SnO_2$ [48], NiO [49] nanorods. Reports on lead oxide ($PbO_2$) [50], chromate ($PbCrO_4$, $CuCrO_4$, $BaCrO_4$) [51], cerium oxide ($CeO_2$) [52] nanorods have also been published recently.

*2.1.2.2.2. Sonochemical method.* Sonochemical method uses ultrasonic wave to acoustically agitate or alter the reaction environment, thus modifies the crystal growth. The sonication process is based on the acoustic cavitation phenomenon which involves the formation, growth, and collapse of many bubbles in the aqueous solution [53]. Extreme reaction conditions can be created at localized spots. Assisted by the extreme conditions, for example, at temperature greater than 5000 K, pressure larger than 500 atm, and cooling rate higher than $10^{10}$ K/s, nanostructures of metal oxides can be formed via chemical reactions. Kumar et al. have synthesized magnetite ($Fe_3O_4$) nanorods in early days by ultrasonically irradiating aqueous iron acetate in the presence of beta-cyclodextrin which serves as a size-stabilizer [54]. Hu et al. later demonstrated that linked ZnO rods can be fabricated by ultrasonic irradiation under ambient conditions and assisted by microwave heating [55]. Recently, nanocomposite materials have been grown by applying this technique; Gao et al. synthesized and characterized ZnO nanorod/CdS nanoparticle (core/shell) composites [56]. Q1D rare earth metal oxides, such as europium oxide ($Eu_2O_3$) nanorods [57] and cerium oxide ($CeO_2$) nanotubes [58], have also been obtained via this method.

*2.1.2.2.3. Hydrothermal.* Hydrothermal process has been carried out to produce crystalline structures since the 1970s. This process begins with aqueous mixture of soluble metal salt (metal and/or metal–organic) of the precursor materials. Usually the mixed solution is placed in an autoclave under elevated temperature and relatively high pressure conditions. Typically, the temperature ranges between 100 °C and 300 °C and the pressure exceeds 1 atm. Many work have been reported to synthesize ZnO nanorods by using wet-chemical hydrothermal approaches [59–61]. Via this technique, other Q1D oxide materials have also been produced, such as CuO [62], cadmium orthosilicate [63], $Ga_2O_3$ [64], $MnO_2$ nanotubes [65], perovskite manganites ($Fe_3O_4$) [66], $CeO_2$ [67], $TiO_2$ [68], and $In_2O_3$ [20].

## 2.2. Vertical and horizontal alignment strategies

In order to fully take the advantage of the geometric anisotropy of Q1D structures for integrated device applications, the control of their location, orientation and packing density is of paramount importance. Since these nanostructures can be grown from catalytic seeds via VLS process, one route to reach this objective is to simply control the locations of the catalysts. In fact, both lithographic (top down) and non-lithographic (bottom-up) techniques have been employed to achieve defined growth of nanostructures. Based on these techniques, vertical as well as horizontal alignment of Q1D metal oxide structures has been accomplished. In many cases, epitaxial substrate/layer is utilized to assist the directional growth of nanostructures. In addition, alignment using template or external field has also achieved. Below several procedures in manipulating the orientation and alignment of nanowires will be described.

*2.2.1. Catalyst patterning*

A simple route leading to the growth of nanowires at the desired location is by catalyst patterning. Lithography and nanoimprint [69] techniques have been widely used to achieve this objective. In general, they refer to photolithography, electron beam lithography and masking methods. By utilizing standard UV exposure, catalyst patterns are easily defined by photolithography with a resolution limit of ~1 μm. For example, square and hexagonal catalyst pattern arrays were generated on sapphire substrate, and ZnO nanowires were grown from the patterned catalysts via a VLS process [22]. On the other hand, due to the high resolution of electron beam, electron beam lithography can achieve more precision in defining catalyst pattern, yielding highly-ordered and high density nanowire array. Another approach is to imprint a mask or to take a ready-to-use patterned structure to serve as shadow masks. This method has attracted interests owing to its low cost and simple implementation. For instance, TEM copper grid has been used as a mask to directly generate pattern for Au catalyst deposition, which results in the growth of ZnO nanowire array [70].

*2.2.2. Substrate lattice matching*

By carefully selecting substrate, Q1D structures can grow epitaxially from the substrate due to the lattice matching between the crystal and the substrate. Using ZnO as an example, in order to grow directional ZnO nanowires, several types of epitaxial substrates have been used, including sapphire [22,23], GaN [71–73], SiC [74], Si [75–77] and ZnO film coated substrates [78]. Among them, the most commonly used epitaxial substrate is sapphire. Johnson et al. have grown vertically aligned ZnO nanowire array on sapphire $(1\,1\,\bar{2}\,0)$ plane, and these vertical nanowires have demonstrated spectacular lasing effect [79]. On the other hand, from the lattice matching aspect, GaN could be an even better candidate since it has the same crystal system and similar lattice constants as ZnO. This has been shown by the work of Fan et al., in which both the sapphire α-plane and GaN (0 0 0 1) plane were used as the epitaxy substrate for ZnO nanowire growth [72]. They discovered that the nanowires grown on GaN epilayer have better vertical alignment than those on sapphire. One additional advantage of applying GaN as epilayer lies in the fact that GaN is much easier to be doped with *p*-type dopants. As a result, the nanoscale light-emitting device based on *n*-ZnO/*p*-GaN heterojunctions is technically more feasible than using *n*-ZnO/*p*-ZnO homojunctions [71].

*2.2.3. Template alignment*

As an alternative to the vertical alignment by lattice matching, using a template to align Q1D metal oxides is a direct route which have many merits. The integration of nanostructures can be easily achieved if the template is precisely designed. A commonly used template is anodic aluminum oxide membrane where the channel density can exceed $10^9$ $cm^{-2}$ by controlling the membrane fabrication procedure which in essence is a self-organizing process. Therefore, there are no costly and complicated lithographic techniques involved. As described in Section 2.1.2, solution phase based method has been utilized to assemble oxide nanowires into AAO by using electrodeposition or sol–gel process. Lately, high density vertical aligned ZnO nanowire array in AAO template was successfully fabricated combining electrochemical deposition and laser ablation-assisted CVD methods. In this method, Sn catalyst is deposited first in AAO using pulsed electrodeposition, then followed by a CVD approach to synthesize the ZnO nanowires [80]. Similar work was also carried out by Liu et al. to realize ZnO intra-nanowire *p*–*n* junction [81]. This work demonstrates the potential of individual vertical nanowire as light-emitting diodes.

*2.2.4. Field alignment*

Applying electric or magnetic field to properly arrange the orientation of nanowires has been explored. Two strategies can be used: applying a field during nanowire synthesis [82] to guide the

growth based on the electric dipole interaction, or applying a field after synthesis to rearrange the position and location of nanowires. The field alignment of carbon nanotubes have been reported [83,84]. As a type of dielectric material, Q1D metal oxides are ideal for electrical alignment. Harnack et al. proposed a wet-chemical synthesis of ZnO nanorods, followed by using an ac electric field at frequency range between 1 kHz and 10 kHz to align the grown nanorods [85]. Similar approach was used in $SnO_2$ nanowire alignment by Kumar et al. [86].

### 2.3. Doping of Q1D metal oxide systems

In order to meet the demand of potential applications offered by metal oxides, both high quality *n*- and *p*-type materials are indispensable. Therefore, it is pivotal to control doping with intrinsic or extrinsic elements to tune their electrical, optical and magnetic properties.

#### 2.3.1. Doping of ZnO nanowires

ZnO is naturally an *n*-type semiconductor due to the presence of intrinsic defects such as oxygen vacancies and Zn interstitials. They form shallow donor levels with ionization energy about 30–60 meV. It has also been suggested that the *n*-type conductivity is due to hydrogen impurity introduced during growth [87,88]. Up to date, various types of dopants, such as group-III (Al [89,90], Ga [91,92], In [92]), group-IV (Sn [92,93]), group-V (N [89,90], P [94], As [95,96], Sb [97]), group-VI (S [16,98]), and transition metal (Co [99], Fe [100], Ni [101], Mn [102]) have been implanted into ZnO nanostructures. Doping group-III and IV elements into ZnO has proved to enhance its *n*-type conductivity. On the other hand, *p*-type ZnO has been investigated by incorporating group-V elements. In addition, co-doping N with group-III elements was found to enhance the incorporation of N acceptors in *p*-ZnO by forming N–III–N complex in ZnO [89,90].

As mentioned above, *n*-type ZnO is easily realized via substituting group-III and IV elements or incorporating excess Zn. By using a so-called vapor trapping configuration, Chang et al. have shown that the electrical properties of ZnO nanowires can be tuned by adjusting synthesis conditions [103] to generate native defects (oxygen vacancy and Zn interstitials). Experimentally, a small quartz vial is used in the CVD system to trap the metal vapor, thus creating a high vapor concentration gradient in the vial. Nanowires were observed to display a variety of morphology at different positions on the growth chip due to the change of Zn and $O_2$ vapor pressure ratio. It was found that those ZnO nanowires grown inside the vial with higher $Zn/O_2$ pressure ratio attains enhanced carrier concentration. As a result, vapor trapping method is an intrinsic doping process which can be used to adjust carrier concentration.

Even though considerable effort has been invested to achieve *p*-type doping of ZnO, the reliable and reproducible *p*-type conductivity has not yet been achieved. The difficulties arise from a few causes. One is the compensation of dopants by energetically favorable native defects such as zinc interstitials or oxygen vacancies. Dopant solubility is another obstacle. An effort to fabricate intra-molecular *p–n* junction on ZnO nanowires was made by Liu et al. [81]. In this work, anodic aluminum membrane was used as a porous template with average pore size around 40 nm. A two step vapor transport growth was applied and boron was introduced as the *p*-type dopant. Consequently, the *I–V* characteristics demonstrated rectifying behavior due to the *p–n* junction within the nanowire. Besides doping ZnO nanowires to *p*-type to fabricate intra-nanowire *p–n* junction, light emission from the *p–n* heterojunctions composed of *n*-ZnO and *p*-GaN has been accomplished [71]. In that work, vertically aligned ZnO nanorod array was epitaxially grown on a *p*-type GaN substrate.

*2.3.2. Magnetic doping of ZnO nanowire*

ZnO emerges as a promising material as dilute magnetic semiconductors (DMS). DMS is attracting tremendous research interests because it is predicted to have high Curie temperature, and can also enhance polarized spin injection into semiconductor systems. Room temperature hole mediated ferromagnetism in ZnO by introducing manganese (Mn) as dopant has been predicted theoretically and reported experimentally by Sharma et al. in ZnO thin film [104]. The effort of growing ferromagnetic $Zn_{1-x}Mn_xO$ ($x = 0.13$) nanowires with Curie temperature of 37 K was reported by Chang et al. [105] (as shown in Fig. 2). Ronning et al. have demonstrated and characterized ZnO nanobelts doped with Mn [102]. Furthermore, ferromagnetism in ZnO nanorods was also observed with Co impurities. Cui and Gibson recently showed the room temperature anisotropic ferromagnetic behavior of Co- and Ni-doped ZnO nanowires [99]. Because of its wide band gap, ferromagnetic ZnO is regarded as an excellent material for short wavelength magneto-optical devices. These studies enable the potential applications of ZnO nanowires as nanoscale spin-based devices.

*2.3.3. Doping of other oxide nanowires*

Besides ZnO, doping of other oxide nanowires have been investigated using various methods. Chang et al. conducted a series of studies on $Ga_2O_3$ nanowires including doping and its effect on transport properties. Before doping, the electron transport measurements demonstrate poor conductivity at room temperature ($10^{-9}\ \Omega^{-1}\ cm^{-1}$). In order to develop practical device application, a *p*-type doping procedure was carried out [21]. Specifically, a thermal diffusion doping process was utilized to substitutionally replace $Ga^{3+}$ ions with $Zn^{2+}$. The resulted conductivity improves by orders of magnitude.

$\alpha$-$Fe_2O_3$ nanostructures have also been studied, showing configurable properties through doping procedures. To control their electrical properties, Q1D $\alpha$-$Fe_2O_3$ nanobelts were doped with elemental Zn. Depending on the doping conditions, $\alpha$-$Fe_2O_3$ nanobelts can be modified to either *p*-type or *n*-type with enhanced conductivity and electron mobility [106]. More discussion will be presented in Section 3.5.

$In_2O_3$ nanowires have been doped with Ga [107] and native defects [108]. By tuning the carrier concentration, electrical transport and gas sensing properties were shown to be optimized [108,109]. In addition, $In_2O_3$ nanowires have been doped with Sn, resulting in indium tin oxide (ITO) nanowires

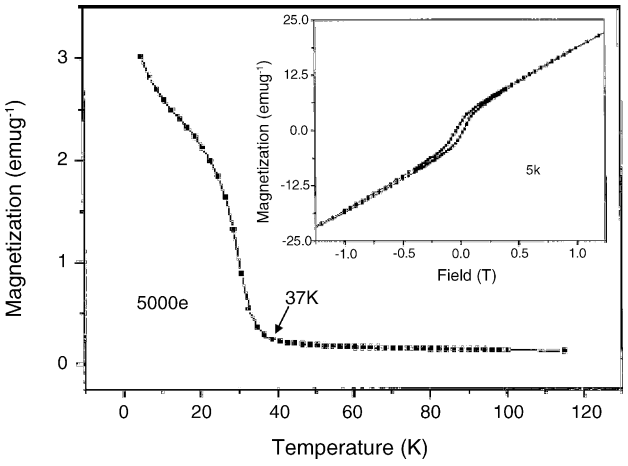


Fig. 2. Temperature-dependent magnetization curve of $Zn_{1-x}Mn_xO$ ($x = 0.13$) nanowire at 500 Oe shows Curie temperature of 37 K. Inset: Magnetization-field hysteresis loop obtained at 5 K (reprint permission from Ref. [105]).

[110,111]. On the other hand, indium doped $SnO_2$ nanowires were also obtained via epitaxial directional growth with indium concentration at ~5% atomic ratio [112].

### 2.4. Construction of nanoscale metal oxide heterostructures

As discussed before, Q1D metal oxides have been grown via various template methods. Interestingly, these Q1D structures themselves can function as templates for growing novel heterostructured materials. These materials can be mainly classified into three configurations: coaxial core–shell nanowires, longitudinal superlattice nanowires, and layered nanotapes, as illustrated in Fig. 3a.

#### 2.4.1. Core–shell nanowires

Semiconductor nanowires have been made into core–sheath configuration [116,117], which permits the formation of heterojunctions with in the nanostructure, yielding tunable and efficient devices [118]. Recently, heterostructured metal oxide nanowires start to attract much attention. Several types of core/shell structure have been synthesized, such as semiconductor/oxide [119], metal/oxide [120], oxide/oxide [114,121,122], oxide/polymer [123], etc. The unique heterojunctions formed at the core/shell interfaces render promising prospect in making functional devices. The investigations of oxide inner–outer shell interactions are still undergoing [116,124]. The outer shell can readily

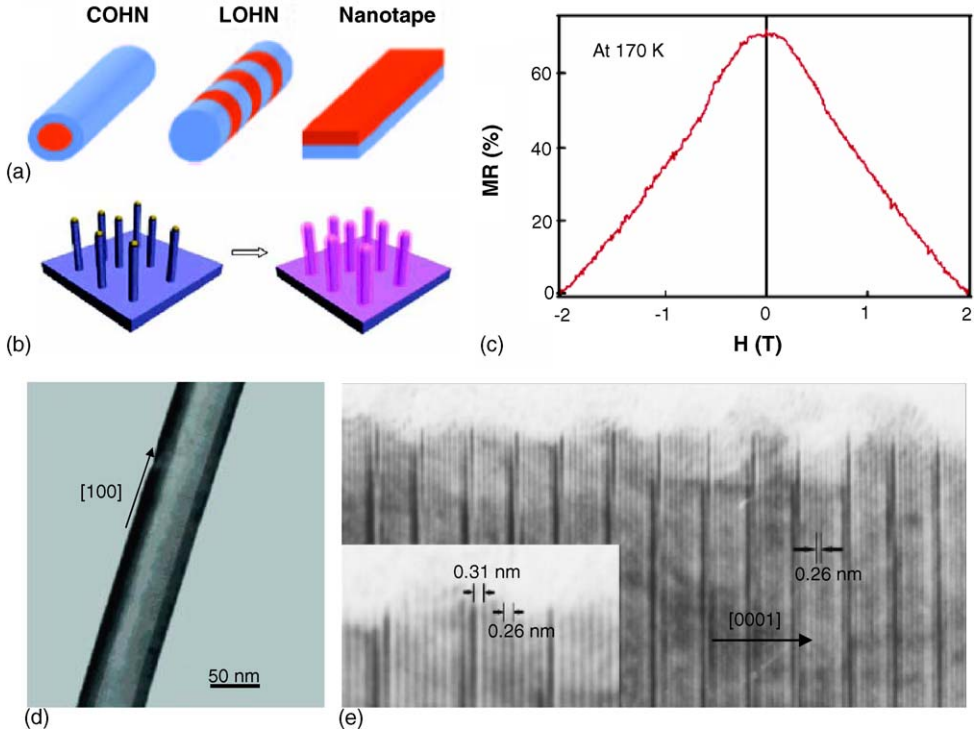


Fig. 3. (a) Three different types of heterostructures using Q1D as template: core–shell heterostructured nanowire (COHN), a longitudinal heterostructured superlattice nanowire (LOHN), and a nanotape (reprint permission from Ref. [113]). (b) Schematic illustration of vertically aligned $Fe_3O_4$ shell coated on MgO core nanowire. (c) Magnetoresistance measured at 170 K with a magnetic field swept from −2 T to 2 T. (d) TEM image of such core–shell $Fe_3O_4$ nanowire (reprint permission from Ref. [114]). (e) HRTEM image of an individual $In_2O_3$/ZnO nanowire with longitudinal superlattice structure (reprint permission from Ref. [115]).

become a nanotube. For instance, amorphous alumina was grown by atomic layer deposition on ZnO nanowires to form ZnO/$Al_2O_3$ core/shell configuration. Individual amorphous $Al_2O_3$ nanotube was then obtained after wet etching the core ZnO material. By selecting proper core material, epitaxial shell growth [114,122] can be realized instead of amorphous deposition. Han et al. used vertically aligned single-crystalline MgO nanowires as Q1D template to produce a variety of transition metal oxide core/shell structured nanowires (Fig. 3b) including $YBa_2Cu_3O_{6.66}$ (YBCO), $La_{0.67}Ca_{0.33}MnO_3$ (LCMO), $PbZr_{0.58}Ti_{0.42}O_3$ (PZT), and $Fe_3O_4$. A significant achievement of 70% magnetoresistance (MR) was observed in MgO/LCMO nanowire system at 170 K (Fig. 3c) [114] and 1.2% MR at room temperature in $Fe_3O_4$/MgO nanowires (Fig. 3d) with the presence of antiphase boundaries [125]. Moreover, sophisticated ZnO/$Mg_{0.2}Zn_{0.8}O$ multishell structure was fabricated for radial direction quantum confinement investigation performed by Jang et al. [126]. In their work, the dominant excitonic emissions in the photoluminescence spectra showed a blue shift which depends on the ZnO shell layer thickness. Furthermore, near-field scanning optical microscopy demonstrated sharp photoluminescence peaks corresponding to the subband levels of the individual nanorod quantum structures.

#### 2.4.2. *Longitudinal superlattice nanowires*

By periodically controlling the growth condition during the synthesis process, longitudinal heterojunctions can be created along the Q1D structure. Longitudinal composition modulated semiconductor nanowires such as GaAs/GaP [127], Si/SiGe [128], and InAs/InP [129] have been obtained. Single or multiple *p–n* junctions of these commonly used semiconductors were formed and characterized. $In_2O_3$/ZnO superlattice structure was introduced by Jie et al. In that work, ZnO, $In_2O_3$, and $Co_2O_3$ mixture were thermally evaporated [115]. The resulting superlattice is $In_2O_3(ZnO)_m$ confirmed by HRTEM, as shown in Fig. 3e. The following works were performed by Na et al. [130]. They showed $In_2O_3(ZnO)_5$ ($a$ = 0.3327 nm, $c$ = 5.811 nm) and $In_2O_3(ZnO)_4$ ($a$ = 0.3339 nm, $c$ = 3.352 nm) two superlattices doped with Sn. The as-fabricated superlattices were compared with the pristine ZnO nanowires in the structure, composition, and optical properties. Electrical measurement of the intra-nanowire *p–n* junctions exhibited rectifying behavior [127]. More importantly, polarized electroluminescence was observed, demonstrating their application as nanoscale light-emitting devices [127].

## 3. Physical properties of Q1D metal oxide nanostructures

As a group of functional materials, metal oxides has a wide range of applications, including transparent electronics, chemical sensors, piezoelectric transducers, light-emitting devices, etc. The down scaling of the material dimension not only implies a shrinkage of the active device which leads to higher packing density and lower power consumption, but also can significantly improve the device performance. In addition, when the dimension reduces to a few nanometers, quantum mechanical effects start to play an important role. Doubtlessly a thorough understanding of the fundamental properties of the Q1D metal oxide system is indisputably the prerequisite of research and development towards practical applications. This section will provide a collection of the physical properties of some representative members in the Q1D metal oxide family, such as ZnO, $In_2O_3$, $Ga_2O_3$, $SnO_2$, $Fe_2O_3$, $Fe_3O_4$, CuO, CdO, $TiO_2$, and $V_2O_5$. The topics in this section will cover some selected properties on crystal structures, electrical conduction, and optical emission. Their device characteristics as field-effect transistors, field emitters, sensors, will be further described in Section 4.

### 3.1. ZnO

As one of the prominent materials in the metal–oxide family, nanostructured zinc oxide (ZnO) has been intensely studied for its versatile physical properties and promising potential for electronics as well as optoelectronics, and piezoelectricity applications. ZnO is a wide bandgap ($E_g$ = 3.4 eV) II–VI compound semiconductor which has a non-centrosymmetric wurtzite structure with polar surfaces. The structure of ZnO can be described as a number of alternating planes composed of tetrahedrally coordinated $O^{2-}$ and $Zn^{2+}$ ions, stacked alternatively along the *c*-axis. The oppositely charged ions produce positively charged (0 0 0 1)–Zn and negatively charged (0 0 0 −1)–O polar surfaces, resulting in a normal dipole moment and spontaneous polarization along the *c*-axis. The polarization effect induces the formation of stripe structure (as displayed in Fig. 4a–d) [131]. As described in Section 2.1 there have been a variety of methods developed to synthesize Q1D ZnO nanostructures. Electron microscopy reveals that in most circumstances, the as-grown Q1D ZnO nanostructures are single crystalline and have well-defined shape with high aspect ratio. HRTEM images shown in Fig. 4e demonstrate the ZnO nanowires obtained by the CVD method [103]. Lattice fringes can be clearly distinguished as 0.52 nm, and the growth direction of the nanowire is [0 0 0 1] confirmed by the selected-area electron diffraction (SAED) pattern (Fig. 4e, right inset).

In order to explore the potential of ZnO nanowires as the building blocks for nanoscale electronics, electrical transport properties of ZnO nanowires have been investigated. It was found that ZnO is a typical *n*-type semiconductor which originates from the native defects such as oxygen vacancies and zinc interstitials. Since the defects are concentrated in the surface region, they have significant effect on the electrical and optical properties of the Q1D structure with a large surface-to-volume ratio [22]. Electrical transport studies after configuring individual ZnO nanowires as field-effect transistors (FET) [132] confirm that they exhibit *n*-type behavior. Typically the field-effect mobility of as-grown nanowires is in the range of 20–100 $cm^2$/V s. It will be shown later in Section 4.1.1 that after surface treatment, the mobility of ZnO nanowires can be dramatically enhanced to exceed 4000 $cm^2$/V s [133].

Optical properties of Q1D ZnO nanostructures have been extensively studied because of their promising potentials in optoelectronics. Compared with other wide bandgap semiconductors, for example GaN, ZnO has a large exciton binding energy (60 meV) which ensures efficient excitonic

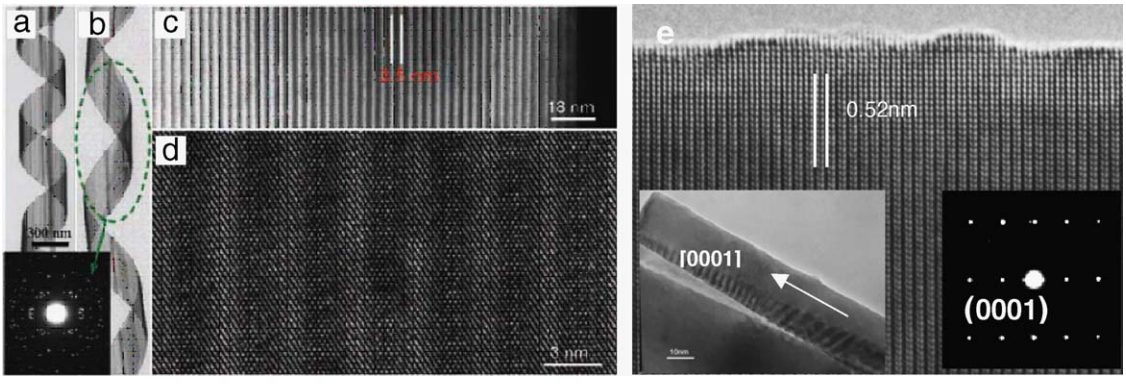


Fig. 4. (a) Typical low-magnification TEM image of a ZnO nanohelix, showing its structural uniformity. (b) Low-magnification TEM image of a ZnO nanohelix with a larger pitch-to-diameter ratio. (c) Dark-field TEM image from a segment of a nanohelix, showing that the nanobelt that coil into a helix is composed of alternatively distributed stripes at a periodicity of 3.5 nm. (d) HRTEM image shows the lattice structure of the two alternating stripes (reprint permission from Ref. [131]). (e) HRTEM image of the edge of the nanowire showing ZnO crystal lattice fringes with spacing of 0.52 nm. The inset is a SAED pattern confirming the growth direction along the [0 0 0 1] *c*-axis (reprint permission from Ref. [103]).

emission at room temperature. Due to its large energy bandgap and exciton binding energy, ZnO is especially suitable for short wavelength optoelectronic applications. Photoluminescence spectra reveal fundamental optical properties of the material, including band-edge emission, defect characterization, exciton–phonon interaction. Fig. 5a demonstrates the photoluminescence of ZnO nanowires with diameters of 100 nm, 50 nm, and 25 nm [22]. Both band-edge emission at ~380 nm and defect state related green emission centering at ~520 nm were observed. The progressive increase of the green emission intensity with a decrease of nanowire diameter suggests that the defect level is higher in thinner nanowires due to the increasing surface-to-volume ratio. Continuous reduction of the diameter of ZnO nanowire results in a quantum size effect which manifests itself in the blue shift of band-edge emission in the photoluminescence spectra (as shown in Fig. 5b) [134]. It has also been reported that the exciton binding energy is significantly enhanced due to size confinement in ZnO nanorods with diameter of ~2 nm [135].

### 3.2. $In_2O_3$

$In_2O_3$ has also attracted considerable research effort. It is known to have a body centered cubic structure ($a$ = 10.12 Å) with a direct bandgap of 3.75 eV [20]. The wide bandgap renders $In_2O_3$ high optical transparency and makes it an important material for transparent conductive electronics. In fact, it has been widely used as window heaters, solar cells, and liquid crystal displays [136].

Nanostructured $In_2O_3$ such as nanowires and nanobelts has been successfully synthesized via both catalyst-free growth and catalyst-assisted VLS processes [107,136–138]. $In_2O_3$ nanowires had also been synthesized by thermal oxidizing In nanowires embedded in AAO grown by electrodeposition process [139,140].

Structural studies using high resolution transmission electron microscopy (HRTEM) reveal that the majority of Q1D $In_2O_3$ nanostructures obtained by catalyst-free CVD process grow along [1 0 0] direction, and some grow along [1 1 0] direction, as indicated in Fig. 6 [136,137].

To characterize the electrical property of $In_2O_3$ nanowires, individual nanowires had been configured as field-effect transistors using photolithography technique [6]. It was observed that oxygen vacancy renders $In_2O_3$ with $n$-type semiconducting behavior. As shown in Fig. 7a, conductance of nanowires increases with the increase of back gate voltage. Using the transconductance

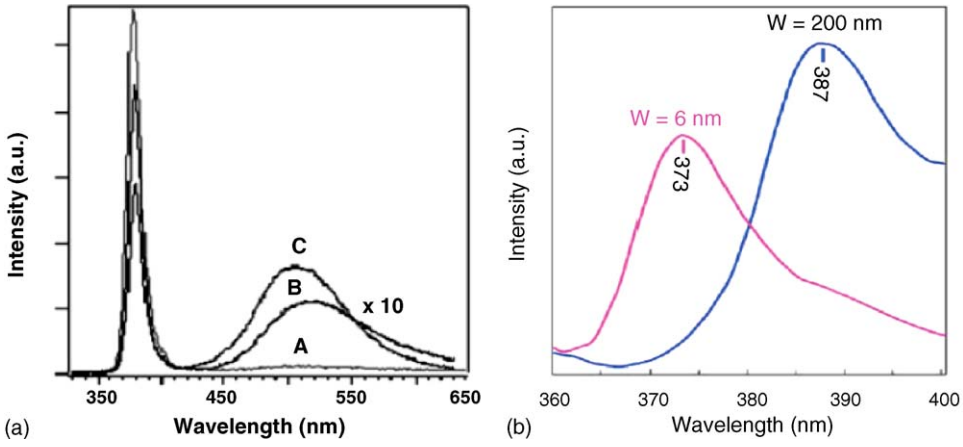


Fig. 5. (a) Photoluminescence of ZnO nanowires with diameters of 100 nm, 50 nm, and 25 nm (reprint permission from Ref. [22]). (b) PL spectra of 6 nm and 200 nm wide ZnO nanobelts showing a blue shift of the emission peak (reprint permission from Ref. [134]).

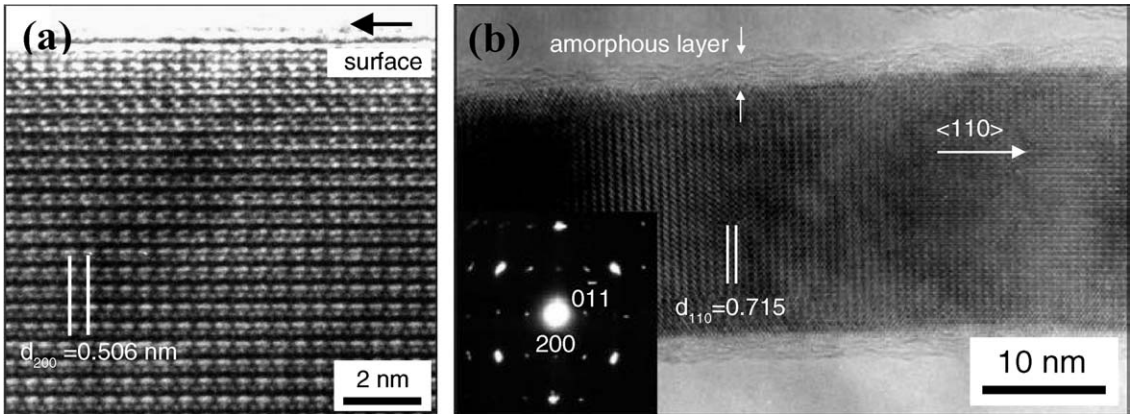


Fig. 6. HRTEM images of two $In_2O_3$ nanobelts grow along (a) [1 0 0] and (b) [1 1 0] direction (reprint permission from Ref. [136]).

obtained from the $I$–$V_g$ curve, an electron mobility of 98.1 $cm^2/V$ s and Q1D carrier concentration of $2.3 \times 10^{-7}$ $cm^{-1}$ were calculated. For $In_2O_3$ nanowires with a diameter of 10 nm, zero-bias anomalies have been measured, following a power-law behavior at large gate voltage. Such observation might show evidence of Luttinger liquid behavior as the carrier density in the nanowire becomes degenerate [141].

Photoluminescence studies demonstrate oxygen vacancy related emission with wavelength ranging from 392 nm to 570 nm [20,136,138,139]. Fig. 7b demonstrates a PL spectrum of $In_2O_3$ obtained at room temperature under excitation at 260 nm [138]. The $In_2O_3$ nanowires emit stable and high intensity blue light with PL peaks at 416 nm and 435 nm. XPS has confirmed the oxygen defects in the nanowires, thus it is believed that the intensive blue light emission is attributed to oxygen vacancies and indium–oxygen vacancy centers. After excitation of the acceptor, a hole on the acceptor $[(V_{In}, V_o)^x]$ and an electron on a donor $[(V_o{}^x)]$ are created according to the following formalism:

$$(V_o, V_{In})' + V_o{}^{\bullet} + h\nu \rightarrow (V_o, V_{In})^x + V_o{}^x$$

The reverse process results in luminescence, which is divided into two steps. First, an electron in donor band is captured by a hole on an acceptor to form a trapped exciton. Second, the trapped exciton recombines radiatively emitting a blue photon [138].

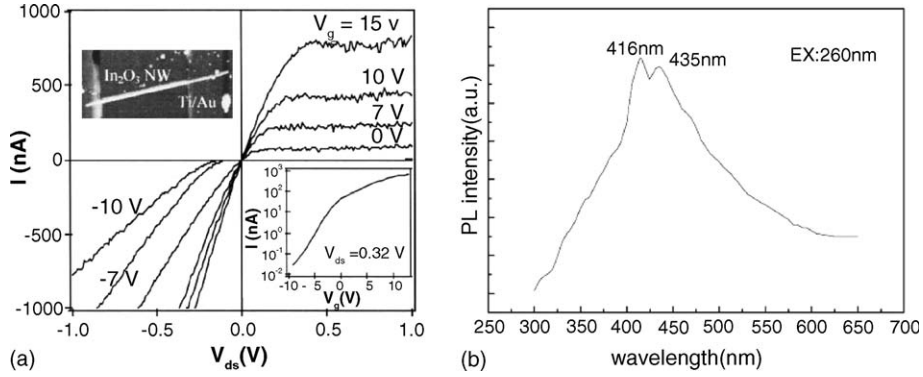


Fig. 7. (a) Gate-dependent $I$–$V$ curves measured at room temperature. The lower inset shows the current vs. gate voltage at $V_{DS}$ = 0.32 V. The gate modulates the current by five orders of magnitude. The upper-left inset is an AFM image of the $In_2O_3$ nanowire between two electrodes (reprint permission from Ref. [6]). (b) Photoluminescence spectra of the $In_2O_3$ nanowires at room temperature under excitation at 260 nm (reprint permission from Ref. [138]).

### 3.3. $Ga_2O_3$

Gallium oxide (β-$Ga_2O_3$) has a monoclinic crystal structure and a wide band gap of 4.9 eV. Its remarkable thermal and chemical stability make it suitable for many applications such as high temperature oxygen sensor [142], magnetic tunnel junction, and UV-transparent conductive material. Q1D structures of $Ga_2O_3$, such as nanowires and nanobelts, have been synthesized and characterized [11,143–148]. In the work performed by Chang et al., a catalytic thermal CVD method is used to grow $Ga_2O_3$ nanowires [21]. The as-grown nanowires were characterized by HRTEM as shown in Fig. 8a and b.

The optical property of $Ga_2O_3$ nanowires has been characterized by photoluminescence [21,143] and catholuminescence [148,149] methods. Because of its large bandgap energy, $Ga_2O_3$ is expected to have deep ultra-violet range optoelectric effect. Most of the investigations show that there is no band to band transition observed. Instead, a broad blue-green emission is observed, as shown in Fig. 8c. This originates from the recombination of an electron on a donor (oxygen vacancies) and a hole on an acceptors (gallium–oxygen vacancy pairs), respectively [21]. These donor–acceptor pairs form trapped excitons resulting in this broad blue-green emission similar to the mechanism of $In_2O_3$. With increasing temperature, this emission can be quenched either by electron detrapping from a donor to the conduction band or by hole detrapping from an acceptor to the valence band.

Recent studies on electrical transport properties have been reported [21,147]. Yu et al. measured the transport properties of nanoribbons and nanowires under vacuum condition [147], and Chang et al. investigated Zn-doped $Ga_2O_3$ nanowire FET performance under air ambient [21].

### 3.4. $SnO_2$

With a wide bandgap energy of 3.6 eV, *n*-type semiconducting $SnO_2$ has been explored and widely used for transparent conductive electronics. Single crystalline $SnO_2$ nanobelts and nanowires are synthesized by thermal evaporation or laser ablation. Alternatively, solution-phase $SnO_2$ synthesis has also been achieved using $SnCl_4$ precursor [150]. High resolution transmission electron microscopy and selected-area electron diffraction (SAED) studies, as shown in Fig. 9a–c, indicate that some $SnO_2$ nanowires have a normal rutile crystal structure ($a$ = 4.70 Å and $c$ = 3.19 Å) and the growth direction is along [1 0 1] direction [19]. In contrast, some of the other $SnO_2$ nanowires display a different crystal

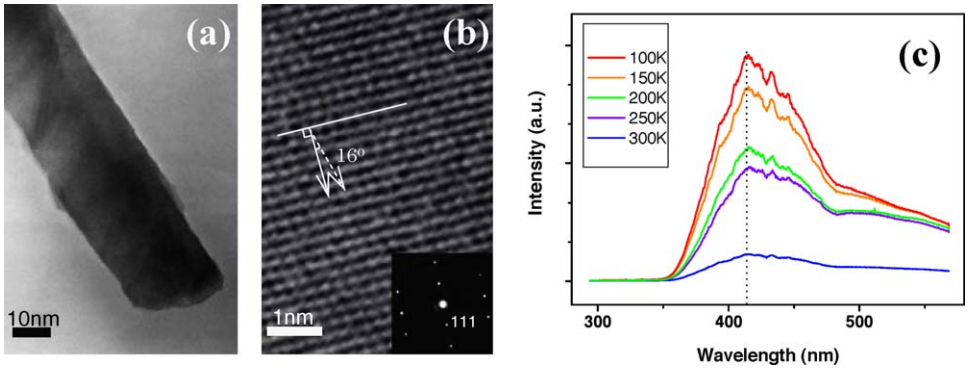


Fig. 8. (a) HRTEM image shows a nanowire with a diameter about 36 nm. (b) The distance between (1 1 1) planes is around 2.55 Å. The angle between the [1 1 1] direction and the long axis of this wire is approximately 16°. (c) Temperature dependence PL shows increased emission intensity at low temperature (reprint permission from Ref. [21]).

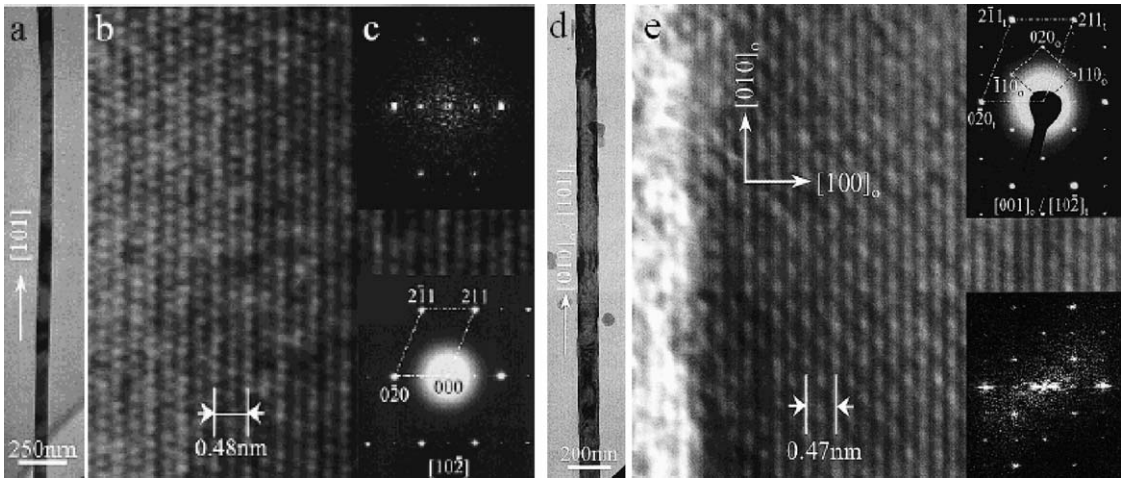


Fig. 9. (a) Low magnification TEM image of a rutile structured $SnO_2$ nanowire. (b) HRTEM image of the nanowire. (c) Corresponding FFT of the image, and SAED pattern from the nanowire. (d) Low magnification TEM image of an individual orthorhombic $SnO_2$ nanowire. (e) The corresponding HRTEM image. The inset at the upper-right-hand corner is a SAED pattern obtained for the nanowire and the inset at the bottom right-hand corner is a FFT of the HRTEM image (reprint permission from Ref. [19]).

structure (Fig. 9d and e), which is determined to match that of orthorhombic structure having the lattice parameters: $a = 4.714$ Å, $b = 5.727$ Å, and $c = 5.214$ Å.

Room temperature PL spectrum shows a strong yellow emission band with the maximum peak at about 570 nm, as shown in Fig. 10a. However, near band-edge emission (∼254 nm) is not detected, similar to the case in $Ga_2O_3$ nanowire [151]. Because of the non-stoichiometry of $SnO_2$, the maximum transition at about 570 nm originates from deep levels within the band gap due to the surface defect states, corresponding to oxygen vacancies or tin interstitials. Electrical transport measurements performed by Liu et al. confirm the *n*-type semiconducting properties of $SnO_2$ nanowires, as shown in Fig. 10b. Electron carrier concentration and mobility of single $SnO_2$ nanowire were estimated to be $1.5 \times 10^8$ cm$^{-1}$ and 40 cm$^2$/V s, respectively.

### 3.5. $Fe_2O_3$

As the most stable iron oxide phase under ambient condition, α-$Fe_2O_3$ ($E_g = 2.2$ eV) is widely used for catalysts, non-linear optics, gas sensors, etc. [152,153]. Q1D nanostructures of α-$Fe_2O_3$ have also triggered considerable interest. In fact, α-$Fe_2O_3$ nanostructures can be grown via simple oxidation of pure iron [154,155]. Wen et al. demonstrated an interesting morphology transition from nanoflakes to nanowires when heating pure iron at 400 °C, 600 °C, 700 °C and 800 °C [154]. Fig. 11 shows a series of TEM images of α-$Fe_2O_3$ nanowires and nanoscrolls grown at 800 °C. On the other hand, Fu et al. reported large arrays of vertically aligned α-$Fe_2O_3$ nanowires grown by heating pure iron in a gas mixture of $CO_2$, $SO_2$, $NO_2$ and $H_2O$ vapor at 540–600 °C [155]. Besides using thermal oxidation of pure iron, α-$Fe_2O_3$ nanobelts and nanotubes were also produced from solution-based wet approaches [156,157]. Wang et al. reported a solution-phase synthesis method to make nanobelts in $FeCl_3 \cdot 6H_2O$ and $Na_2CO_3$. After a series of heat treatment, single crystal α-$Fe_2O_3$ nanobelts were obtained. Nanotubes had also been grown via a hydrothermal method, and in this case $FeCl_3$ and $NH_4H_2PO_4$ were used instead. The formation mechanism of tubular-structured α-$Fe_2O_3$ has been proposed as a coordination-assisted dissolution process. The presence of phosphate ions

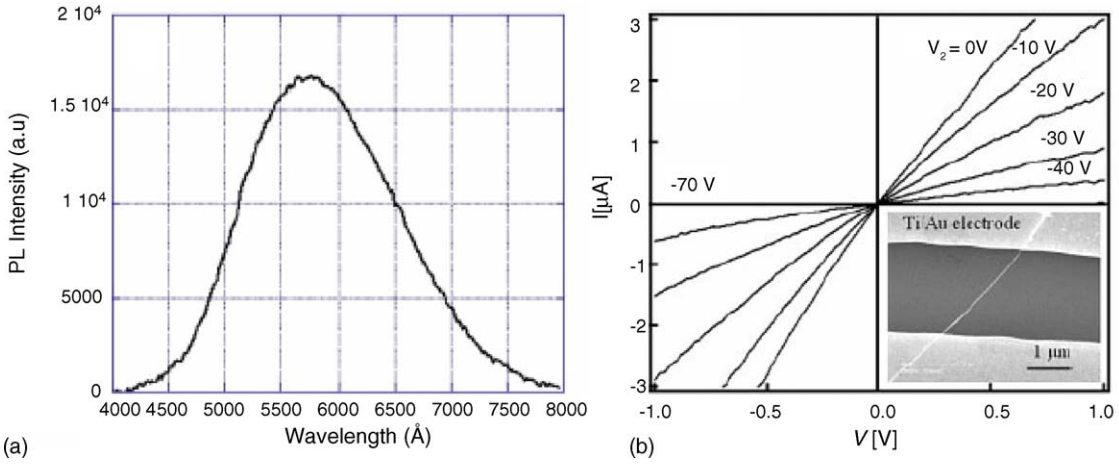


Fig. 10. (a) Room temperature PL spectrum of a large area (3 mm × 3 mm) nanobelts and nanowires array grown on sapphire substrates (reprint permission from Ref. [151]). (b) Gate-dependent *I–V* curve of $SnO_2$ nanowires obtained at room temperature. Inset: SEM image of a $SnO_2$ nanowire between two Au–Ti electrodes (reprint permission from Ref. [7]).

used in this process is crucial for the tubular structure formation, which results from the selective adsorption of phosphate ions on the surfaces of hematite particles and their ability to coordinate with ferric ions.

The electrical transport properties of α-$Fe_2O_3$ nanobelts were investigated by Fan et al. [106]. It was found that similar to ZnO and $In_2O_3$, native oxygen vacancy renders α-$Fe_2O_3$ nanobelts *n*-type semiconducting behavior, as shown in Fig. 12a. However, in contrast to ZnO and $In_2O_3$, experiments showed that α-$Fe_2O_3$ nanobelts can be easily doped with Zn and converted to *p*-type at 700 °C. Fig. 12b plots the *p*-type *I–V* characteristic. This *p*-type doping effect was attributed to the substitution of $Fe^{3+}$ by $Zn^{2+}$ions. The doping effect on the initial *n*-type behavior changing to *p*-type also manifests itself in the modification of the contact property, as observed in the increasingly non-linear *I–V* curves shown in Fig. 12. On the other hand, when the doping process was carried out at lower temperature, enhanced *n*-type behavior was observed with higher conductivity and mobility.

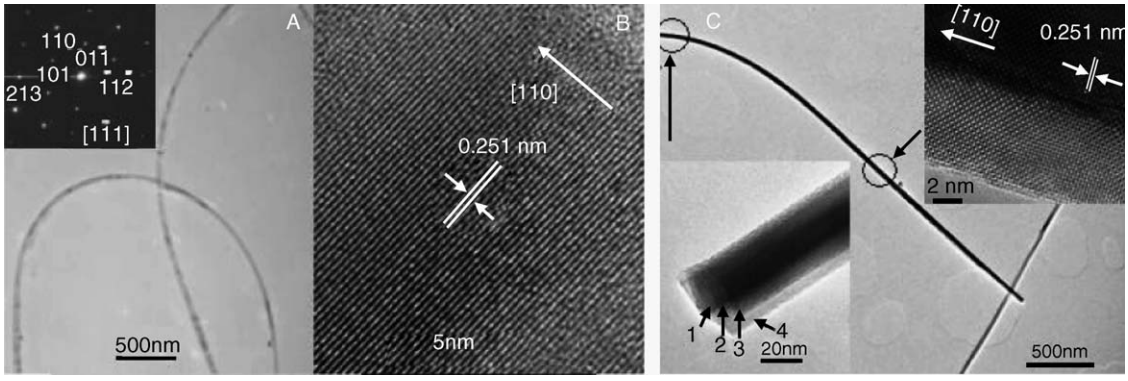


Fig. 11. (a) Low-magnification TEM image of the nanowires with an electron diffraction pattern of a single α-$Fe_2O_3$ nanwire (inset). (b) HRTEM image shows growth direction [1 1 0] with lattice spacing 0.251 nm. (c) Low-magnification TEM image of a single nanoscroll. Bottom left inset: high-magnification TEM image of the nanoscroll tip. Top right inset: HRTEM image of the same nanoscroll in the shaft region (reprint permission from Ref. [154]).

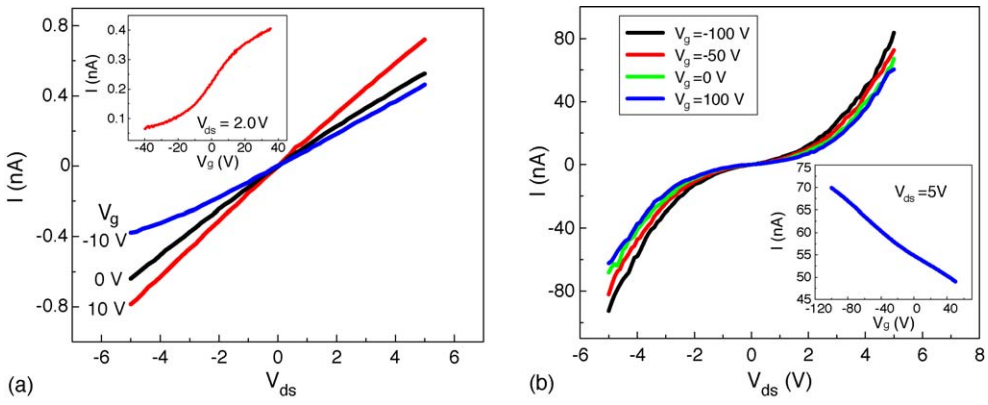


Fig. 12. (a) *I–V* characteristics of an *n*-type α-$Fe_2O_3$ nanobelt FET obtained at back gate potentials of −10 V, 0 V, and 10 V. Inset: $I–V_g$ curve of the nanobelt FET obtained at 2.0 V drain–source bias. (b) *I–V* curves and $I–V_g$ curve (inset) show *p*-type behavior after doping the α-$Fe_2O_3$ nanobelt at high temperature (reprint permission from Ref. [106]).

### 3.6. $Fe_3O_4$

$Fe_3O_4$ nanorods/nanowires have been introduced for ferromagnetic studies [34,158]. Specifically, $Fe_3O_4$ nanowire arrays with an average diameter of about 120 nm and lengths up to 8 μm were synthesized in anodic aluminum oxide templates through electrodeposition and heat treatment of a precursor β-FeOOH. Hysteresis loops measured at room temperature show a clear magnetic anisotropy, as shown in Fig. 13 [34]. Iron-based multi-compound oxide materials such as $CoFe_2O_4$ [159], $MnFe_2O_4$ [160], $NiFe_2O_4$ [161] have also been obtained in Q1D structures.

### 3.7. CuO

Copper oxide (CuO) is a *p*-type semiconductor with a narrow band gap (1.2 eV) which exhibits a number of interesting properties. CuO has been extensively studied because of its close connection to high-$T_c$ superconductors. It can be used as an efficient heterogeneous catalyst to convert hydrocarbons

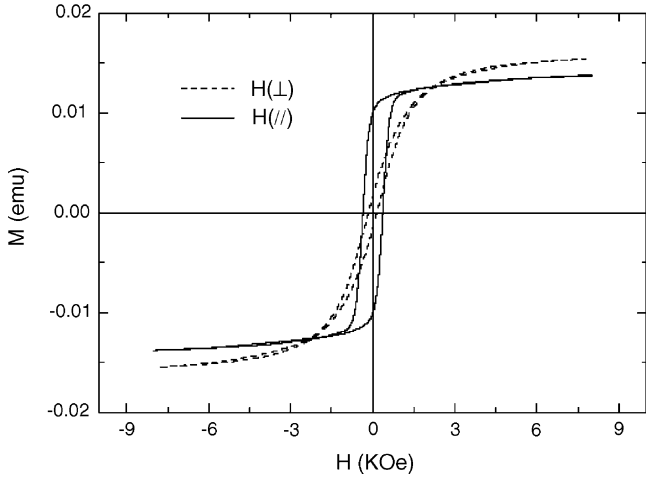


Fig. 13. Hysteresis loops of $Fe_3O_4$ nanowires measured at room temperature, where *H*(//) and *H*(⊥) are the fields applied parallel and perpendicular to the nanowire axes, respectively (reprint permission from Ref. [34]).

completely into carbon dioxide and water [162]. The CuO Q1D structures demonstrate to be efficient electron field emitters [163].

Recently, in the past few years, many methods have been developed to fabricate copper oxide nanowires [70,164]. Xia et al. described a vapor-phase approach to the synthesis of CuO nanowires supported on the surfaces of various copper substrates that include grids, foils, and wires. Fig. 14a–c demonstrates that each CuO nanowire grown on a TEM grid is a bicrystal divided by a (1 1 1) twin plane in the middle along the longitudinal axis.

### 3.8. CdO

Among transparent conductive oxide (TCO) materials, CdO shows promising prospect [165]. As an *n*-type semiconductor, it has a direct band gap of 2.28 eV and an in indirect band gap of 0.55 eV. As mentioned before, several synthesis methods to grow Q1D CdO structure have been developed. Fig. 15a shows a SAED pattern and a TEM image obtained from a single CdO nanoneedle grown by VLS CVD process [8]. The SAED pattern reveals that the CdO nanoneedles have a cubic crystal structure with a lattice constant of 0.47 nm growing along the [2 2 0] direction.

The electrical transport property of the CdO nanoneedles was studied by fabricating electrodes onto individual nanoneedles, as shown in Fig. 15b (inset) [8]. Electrical property was measured at different temperatures, showing that the transport is dominated by thermal emission at high temperatures (as plotted in Fig. 15b). At room temperature the resistivity is found to be $2.25 \times 10^{-4}\ \Omega$ cm, and the electron concentration was estimated to be $1.29 \times 10^{20}\ \mathrm{cm}^{-3}$.

### 3.9. $TiO_2$

$TiO_2$ is an *n*-type semiconductor and has been used in artificial pigments and photosensitizer for photovoltaic cells because of its photocatalytic properties. Q1D $TiO_2$ nanostructures are normally

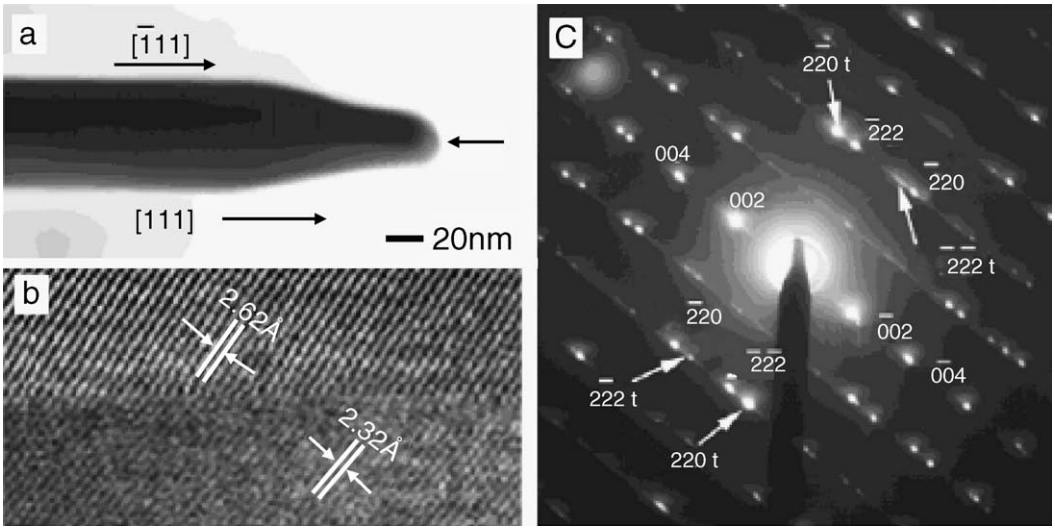


Fig. 14. (a) TEM image of an individual CuO nanowire showing the twin plane in the middle of the wire (indicated by an arrow). (b) HRTEM image shows the twin boundary of a nanowire. (c) Electron diffraction pattern recorded from an individual CuO nanowire. Indices without subscript '*t*' refer to the upper side of the nanowire shown in (b), The electron beam was incident parallel to the [1 1 0] axis. These results indicate that each CuO nanowire is a bicrystal (reprint permission from Ref. [70]).

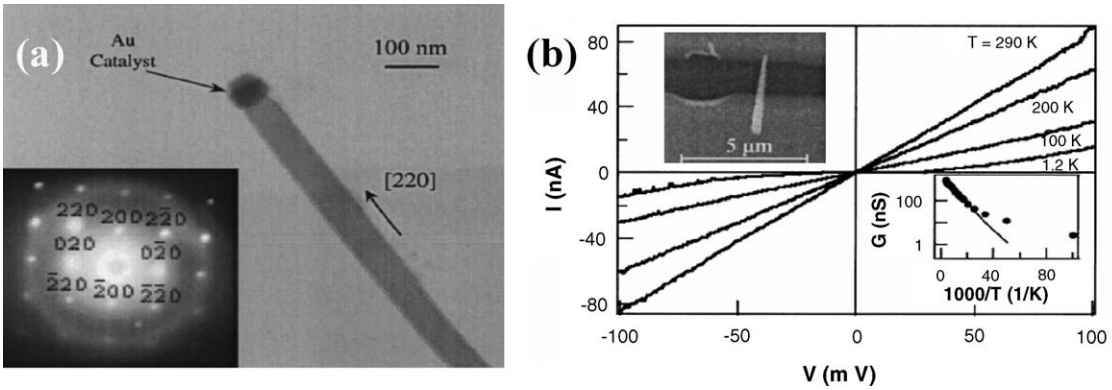


Fig. 15. (a) TEM image of a CdO nanoneedle with a catalyst particle at the very tip. Inset: SAED pattern of the CdO nanoneedle indicating the single crystalline nature. (b) Temperature-dependent *I–V* curves recorded at temperatures ranging from 290 K to 1.2 K. Upper-left inset: SEM image of a CdO nanoneedle between two Au/Ti electrodes. Lower-right inset: conductance (in log scale) as a function of inverse temperature reveals that thermal emission dominates at high temperatures (reprint permission from Ref. [8]).

produced from solution-phase growth methods including surfactant [166], sol–gel [167,168], electrospinning [169], hydrothermal [170,171], etc. The as synthesized $TiO_2$ nanowires often appear in rutile ($a$ = 4.953 Å; $c$ = 2.958 Å) and anatase ($a$ = 3.78 Å; $c$ = 9.498 Å) crystal structures, as shown in Fig. 16a–d.

Recently, thermal evaporation resulted single crystalline $TiO_2$ nanowires has been reported [18,172]. Wen et al. introduced silver (Ag) into solvothermal synthesis and created longitudinal

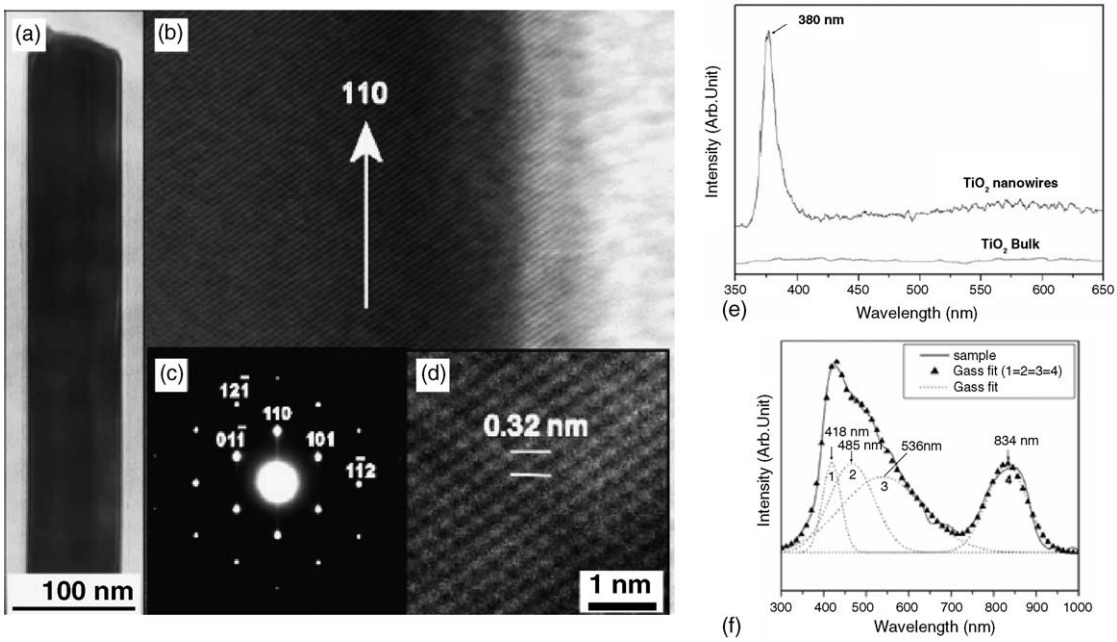


Fig. 16. (a) HRTEM shows an individual $TiO_2$ nanowire. (b) Lattice fringe of the wire indicates growth direction along [1 1 0]. (c) The SAED measurement of (1 1 0) plane shows that the nanowire is perfect single crystalline. (d) This corresponds to the rutile structures, which are the parallel fringes with the spacing of 0.32 nm. (e) PL spectra showing a strong emission peak at approximately 380 nm. (f) CL spectra of $TiO_2$ nanowires at room temperature. The peaks are located at the wavelength 418 nm, 465 nm, 536 nm, and 834 nm, respectively (reprint permission from Ref. [18,172]).

heterojunctions along the Q1D bamboo-like $TiO_2$ nanowires [171]. Due to its potential photocatalytic applications, optical properties of $TiO_2$ nanowires have been characterized [18,172]. In photoluminescence (PL) studies, with incident excitation of 245 nm, single crystal $TiO_2$ nanowires show a peak at 380 nm (Fig. 16e) which results from free exciton emission. Catholuminescence (CL) results (Fig. 16f) show similar result as that of bulk materials. A near IR peak located at 824 nm which represents luminescence transitions of $Ti^{3+}$ interstitial defect states. It is suggested that thermally grown nanowires have similar photocatalytic activities as bulk anatase $TiO_2$ [18]. Additionally, a unique application of the $TiO_2$ nanowires is that the lithium ions can be intercalated into the nanowire and thus form a lithium ion storage system. This $Li^+$ storage capability can be implemented into rechargeable batteries [170,173].

### 3.10. $V_2O_5$

With a band gap of $\sim 2.3$ eV, vanadium pentoxide ($V_2O_5$) attracts much attention for its applications in electrochemistry and spintronics. $V_2O_5$ nanowires and nanotubes have been prepared by several solution based methods [174–176]. Structural analyses suggest that the growth direction of $V_2O_5$ single-crystalline nanowires is along [0 1 0], as shown in Fig. 17.

Optical properties and electrical transport properties of Q1D $V_2O_5$ have been characterized [175,177]. It was found that the conductivity of individual $V_2O_5$ nanowires is around 0.5 S $cm^{-1}$ and the dominant conduction mechanism is polaron hopping [175]. To understand the conduction mechanism, electrical transport measurements have been performed at room temperature and at liquid helium temperature. Results show that thermally activated hopping process increases the conductance as temperature increases.

$V_2O_5$ exhibits remarkable electrochemical properties. It can be used as pseudocapacitor, electrochromic coating and actuators [174,176,178]. As a matter of fact, $V_2O_5$ is usually regarded as an ideal electrode material for lithium ion ($Li^+$) intercalation in Li-based battery [179]. In this case, electrical energy is stored when $V_2O_5$ intercalates $Li^+$, and released when $Li^+$ diffuses out. Since large $V_2O_5$ electrode area increases energy storage capacity of the batteries, the porous structured $V_2O_5$, such as xerogel and aerogel, have been examined. However, these porous structures suffer from the structural instability which hinders their applications. In contrast, nanostructured $V_2O_5$ offers not only large surface area but also robustness, thus rendering a promising solution. The electrochemical

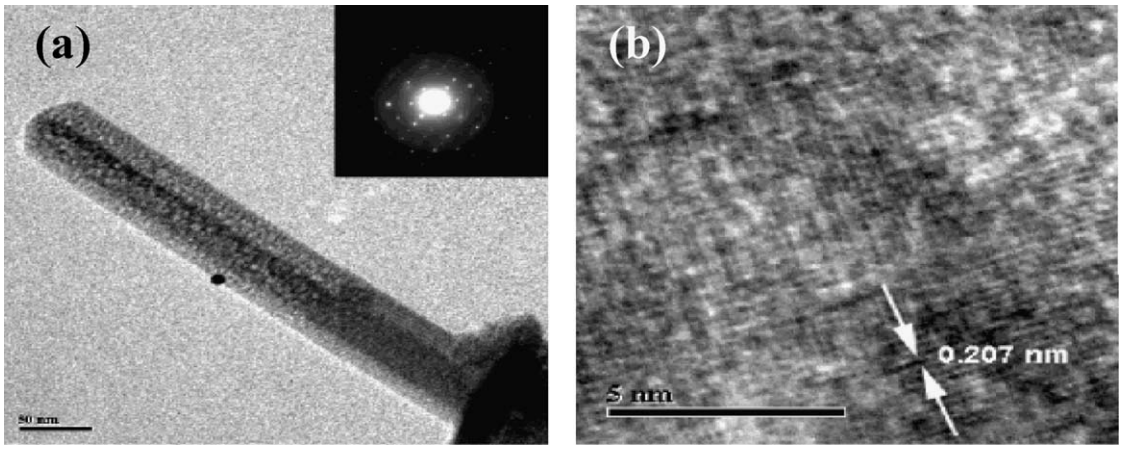


Fig. 17. (a) TEM images of a $V_2O_5$ nanowire grown into a 200 nm membrane and its electron diffraction pattern. (b) HRTEM shows a lattice spacing 0.207 nm and the growth direction is along [0 1 0] (reprint permission from Ref. [176]).

property of $V_2O_5$ nanorod array has been investigated and it has demonstrated considerably improved energy storage capacity compared with both thin film and porous electrode [178].

## 4. Novel nanoscale devices constructed from Q1D metal oxide

The advance of microelectronics technology has been driven by the thrust of fabricating increasingly smaller devices to create integrated circuits with improved performance and architecture. However, while continuously miniaturizing devices dimension, the existing technologies are approaching their physical limits and inevitably looking for alternative breakthroughs. Bottom-up assembly as described in Section 2 has demonstrated the capability to produce submicron, nanoscale features, thus offering new opportunities to complement the CMOS technology. As the potential building blocks for future electronics, Q1D nanosystems exhibit unique physical properties due to it size and structure anisotropy. These properties have been exploited to design and develop various electronic, optoelectronic and mechanical devices. In this context, Q1D nanostructures represent an ideal channel for electrical carrier transport and are suitable for device integration. In this section, applications based on their electrical, optical, and mechanical properties will be reviewed. Specifically, nanoscale electronic devices such as field-effect transistor, light emitter and detector, cantilever, and chemical sensor will be presented.

### *4.1. Tunable electronic devices*

#### *4.1.1. Field-effect transistors*

Q1D structures have been fabricated into field-effect transistors to serve as the fundamental building blocks of electronic devices such as logic gate, computing circuits and chemical sensors. Various metal oxides including ZnO [132], $Fe_2O_3$ [106], $In_2O_3$ [6], $SnO_2$ [7], $Ga_2O_3$ [21], $V_2O_5$ [175] and CdO [8] have been configured to FET. In brief, the fabrication process can be described as following. Nanowires are first dispersed in a solvent, usually isopropanol alcohol or ethanol to form a suspension phase, and then deposited onto a $SiO_2$/Si substrate. The bottom substrate underneath the $SiO_2$ layer is degenerately doped ($p^{++}$ or $n^{++}$), serving as the back gate. Photolithography or ebeam-lithography is utilized to define the contact electrode pattern. Assuming a cylindrical wire of radius $r$ and length $L$, the capacitance per unit length with respect to the back gate may be simply represented as:

$$\frac{C}{L} = \frac{2\pi\varepsilon\varepsilon_0}{\ln(2h/r)}$$

where $\varepsilon$ is the dielectric constant of the gate oxide, and $h$ is the thickness of the oxide layer. From a well-defined transfer characteristics, one can estimate the Q1D carrier concentration and mobility using two simple relations [180]:

$$\text{Carrier concentration}: \quad n = \frac{V_g(th)}{e} \times \frac{C}{L}$$

$$\text{Carrier mobility}: \quad \mu_e = \frac{\mathrm{d}I}{\mathrm{d}V_g} \times \frac{L^2}{CV_{\mathrm{d}s}}$$

$V_g(th)$ is the gate threshold voltage at which the carriers in the channel are completely depleted, $\mathrm{d}I/\mathrm{d}V_g$ denotes the transconductance.

Zinc oxide nanowires and nanobelts have been intensively studied and fabricated into FET for electrical transport measurements. Fig. 18a plots drain–source $I_{DS}$–$V_{DS}$ characteristics at different gate bias of a ZnO FET contacted by Ti/Au electrodes, exhibiting high conductance, excellent gate dependence and high on/off ratio. It is worth noting that the CVD grown ZnO nanostructures are single crystalline, rendering them with superior electrical property to polycrystalline thin film. For example, an electron field-effect mobility of 7 $cm^2$/V s is regarded high for ZnO thin film transistors [181]. However, Park et al. have reported an electron mobility of 1000 $cm^2$/V s after coating the nanowires with polyimide passivation layer to reduce the electron scattering and trapping at surface [182]. Lately, it has been discovered that after coating the ZnO nanowire with a layer of $SiO_2$ followed by $Si_3N_4$ to passivate the surface states, field-effect mobility is dramatically improved and exceed 4000 $cm^2$/V s (as illustrated in Fig. 18). These results indicate that the ZnO Q1D device has exceptional potential in high speed electronics application [133].

### *4.1.2. Vertical electronic device*

In order to increase the integration density of nanoscale devices and fully utilize the scaling advantage, large effort has been conducted to build vertical FETs. A vertical surround-gate nanowire FET was first fabricated by Ng et al. [74]. In this work, the positions of nanowires were controlled via lithographic patterning technique. Vertical aligned ZnO nanowires were observed to grow from lithographically patterned Au spots. These vertical nanowires were then surrounded with $SiO_2$ and Cr which functions as the gate oxide and gate electrode, respectively, as illustrated in Fig. 19a. Fig. 19b shows the drain current versus absolute deviation of gate voltage ($V_{gs}$) from threshold voltage ($V_{th}$) for both *n*-channel and *p*-channel vertical surrounding gate VSG-FETs. The *n*-channel VSG-FET shows a linear dependence while the *p*-channel shows strong non-linearity. This is because that in the *n*-channel, the variation of gate-induced charge involves essentially electrons that are mobile in the channel; whereas in the *p*-channel, the gate-induced charge involves both holes and ionized impurities in the depletion region, and the hole concentration governs conduction and increases with the gate deviation.

The same group has also demonstrated another type of vertical FET based on aligned $In_2O_3$ nanowires [183]. Instead of using conductive SiC substrate, direct electrical contact is made by a self-assembled underlying $In_2O_3$ buffer layer. This buffer layer was formed during the synthesis process right on top of the non-conductive sapphire substrate. This depletion mode *n*-type $In_2O_3$ nanowire vertical FET architecture uses a top-gate configuration which places the gate dielectric capping on the

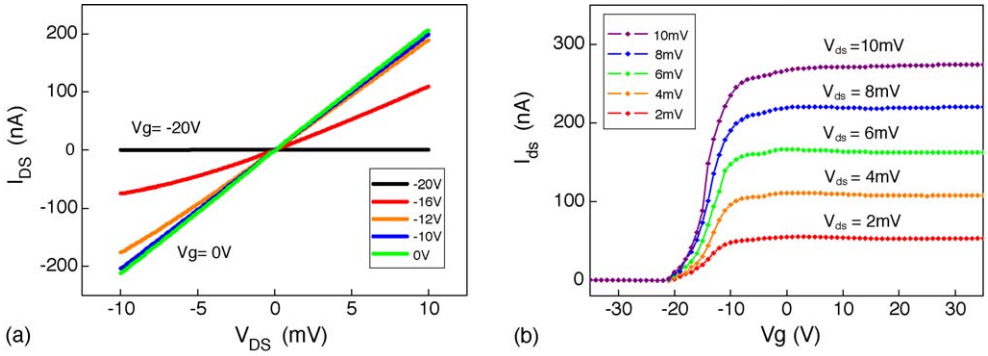


Fig. 18. (a) Current vs. bias voltage (*I–V*) shows *n*-type behavior of ZnO NWFET. Increasing gate voltage contributes to higher conductivity of nanowire. (b) Typical FET current vs. gate voltage ($I$–$V_g$) data shows high performance device behavior (reprint permission from Ref. [133]).

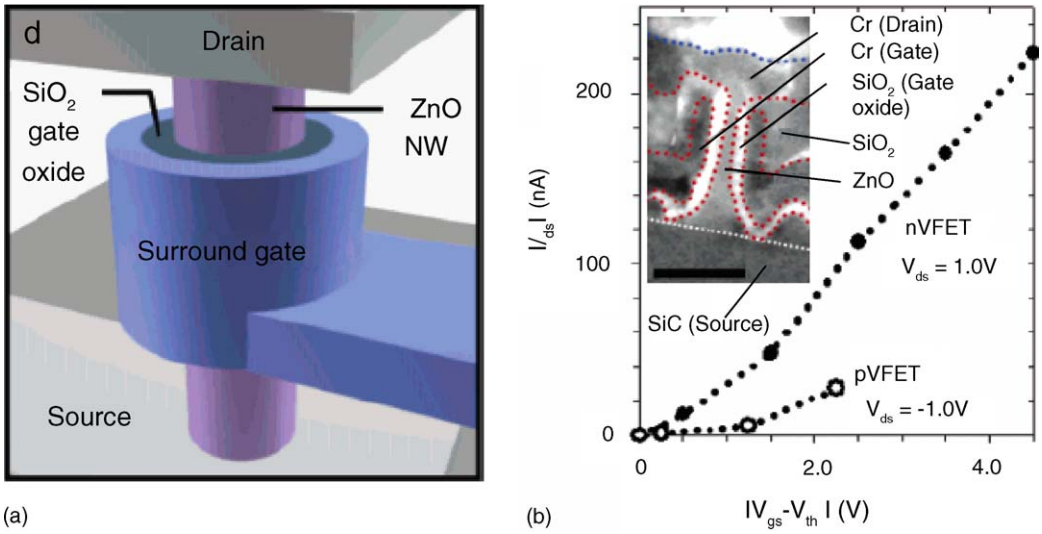


Fig. 19. (a) A 3D schematic illustrating the critical components of a VSG-FET. (b) *I–V* characteristics for two *n*- and *p*-channel VSG-FETs. The inset shows a cross-sectional image of a VSG-FET with a channel length about 200 nm. Scale bar: 200 nm (reprint permission from Ref. [74]).

Pt electrode. These successes in fabricating vertical nano devices can lead to the integration of electronic and optoelectronic devices with high packing density, design flexibility, and function modularity.

### *4.1.3. Field emission tip*

Field emission is an electron escape process from the surface of material under the presence of sufficiently large electric field. The emitting material/electrode is called a cathode that is usually of low electron affinity. Since the discovery of excellent field-emission (FE) properties of carbon nanotubes, there has been a surge of interest in studying field emission of Q1D structures for potential FE applications due to their high aspect ratio. In the last few years, semiconducting Q1D materials start to attract considerable interest for their unique FE properties. Theoretical modeling has elucidated its advantages [184] such as well-controlled electronic properties and low electron affinity. A breakthrough of FE studies using metal oxide nanowires was reported [185] by Lee et al. The aligned ZnO nanowire field emitter demonstrates a turn-on voltage of 6.0 V/μm at a current density of 0.1 μA $cm^{-2}$. The emission current density from the ZnO nanowires reached 1 μA $cm^{-2}$ at a bias field of 11.0 V/μm, which is sufficiently bright for flat panel display application. Since vertically aligned nanowires present lower field threshold (turn-on) with better performance, an assortment of aligned metal oxide Q1D structures, including $IrO_2$ [186], $RuO_2$ [187], $SnO_2$ [188], $In_2O_3$ [189], $WO_3$ [190], $TiO_2$ [191], CuO [163], etc., have been investigated for their FE properties. Moreover, patterning and alignment techniques are applied in fabricating nanowire FE devices [186,189]. In addition other methods, such as surface coating and doping, were also proposed to enhance the performance and efficiency of their field emission property. FE current density is shown to increase and the threshold electric field is reduced by coating a layer of low work function materials such as amorphous carbon and carbon nitride [192]. Sn [93] and Ga [193] doped ZnO has demonstrated lower turn-on electric field. Furthermore, since a drawback of using metal oxide materials for field-emission lies in the surface defect states which trap charge carriers and form high potential barrier, thermal annealing process is used to improve crystal stoichiometry, giving rise to a reduction of surface barrier height and turn-on electric field [187,194].

#### 4.1.4. Logic gate

Diodes and field-effect transistors with electrically controlled ''on'' and ''off'' switching function are the fundamental elements to construct higher level circuits, for instance, logic gates, which are the key components in integrated computation circuit. The transistor function of metal oxide Q1D system has been confirmed in the electrical transport studies. Park et al. have designed and fabricated ''OR'', ''AND'', ''NOT'' and ''NOR'' logic units with *n*-type ZnO nanorods [195]. These gates are built upon a combination of metal–semiconductor Schottky junction diodes or field-effect transistors, as shown in Fig. 20.

### 4.2. Optoelectronics

#### 4.2.1. Emitter, laser, and waveguide

Due to its large energy bandgap and exciton binding energy, ZnO is especially suitable for short wavelength optoelectronic applications. The excitonic recombination provides an efficient radiative process and facilitates a low-threshold stimulated emission. Photoluminescence spectra studies show that ZnO nanowire is a promising material for ultra-violet emission and lasing. Because of its near-cylindrical geometry and large refractive index (∼2.0), ZnO is a natural candidate for optical

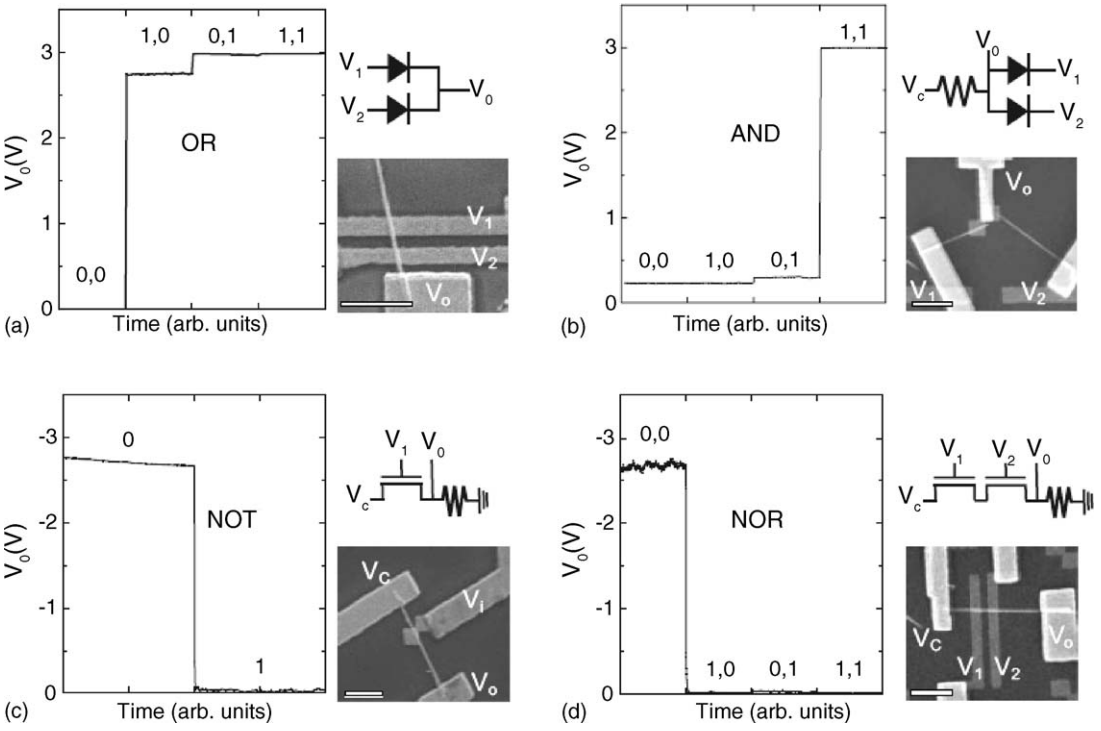


Fig. 20. ZnO nanorod logic devices. (a) Schematic, SEM image, and device characteristic of an OR logic gate fabricated using two Schottky diodes based on a single nanorod. The output voltage ($V_o$) vs. the logic input configurations ($V_1$, $V_2$): (0, 0), (1, 0), (0, 1) and (1, 1). Logic input 0 is 0 V and logic input 1 is 3 V. (b) An AND logic device fabricated using two Schottky diodes based on two ZnO nanorods. For this measurement, $V_c$ is biased at 3 V. (c) A NOT logic gate constructed using a field-effect transistor based on a single nanorod. The output voltage ($V_o$) vs. the logic inputs ($V_i$) of 0 and 1, where logic inputs 0 and 1 are 0 V and −3 V, respectively. $V_c$ is biased at −3 V. (d) A NOR gate using two FETs fabricated on a ZnO nanorod. Voltage bias is the same as for the NOT gate. Scale bars are 2 μm (reprint permission from Ref. [195]).

waveguide. In the work by Law et al. [196], optically pumped light emission is guided by ZnO nanowire and coupled into $SnO_2$ nanoribbon (Fig. 21a and b). In addition, the well-facetted nanowires form ideal optical resonance cavities which facilitate highly directional lasing at room temperature in well-aligned ZnO nanowires [22,197]. Atypical lasing peak is shown in Fig. 21c. To reveal the dynamics underlying the lasing phenomenon, Johnson et al. have used time-resolved second-harmonic generation (TRSHG) and transient PL spectroscopy to probe the creation and relaxation of excited carriers, and successfully described the radiative and non-radiative recombinations [79]. Also in their work, a lasing power threshold of 40–100 kW $cm^{-2}$ is reported and it is suggested that higher crystal quality renders lower threshold. The additional advantage of ZnO nanowire lasers is that the size confinement yields a substantial density of states at the band-edge thus enhances optical gain.

#### 4.2.2. Light-emitting diode

As discussed in the above section, metal oxide nanowire arrays have demonstrated unique UV emitting and even lasing behavior under the excitation of external laser source. However, from the device application point of view, the electrical driven light emitting and lasing are of more technical importance. To achieve this objective, both electrons and holes need to be injected into metal oxide nanostructure to facilitate electron–hole pair recombination. This picture is quite alluring but in the case of ZnO, the fabrication of *p–n* junction is rather difficult for the reason mentioned in Section 2.3.1. Though *p*-type doping presents a hurdle, progress has been achieved on thin film ZnO *p–n* junction for light-emitting diode (LED [198,199]) by introducing nitrogen as the *p*-type dopants. In fact, the intra-molecular *p–n* junctions using ZnO nanowires had been fabricated by Liu et al., however, light emission was not reported [81]. As an alternative solution, light emission from *p–n* heterojunctions composed of *n*-ZnO and *p*-GaN has achieved great success [71]. In this work, vertically aligned ZnO nanorod array was epitaxially grown on a *p*-type GaN substrate (Fig. 22a). The electroluminescence (EL) was measured at room temperature, as shown in Fig. 22b. Another work had reported *p–n* heterojunction formed between ZnO nanowires and *p*-type poly(3,4-ethylenedioxythiophene) (PEDOT)/poly(styrenesulfonate) [200]. Their EL spectrum showed excitonic luminescence at around 380 nm.

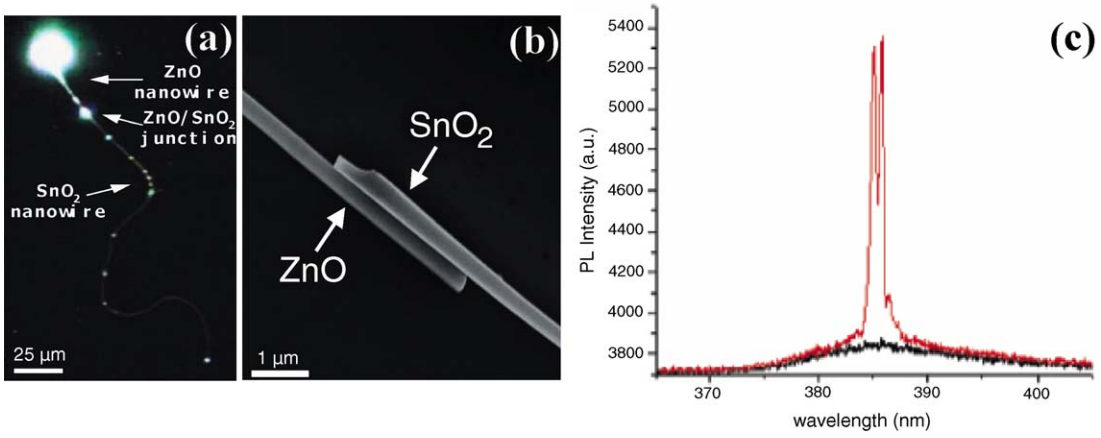


Fig. 21. (a) An optical microscope image of a ZnO nanowire guiding light into a $SnO_2$ nanoribbon and (b) an SEM image displaying the nanowire–nanoribbon junction (reprint permission from Ref. [196]). (c) Stimulated emission of ZnO nanowire laser cavity was observed (reprint permission from Ref. [197]).

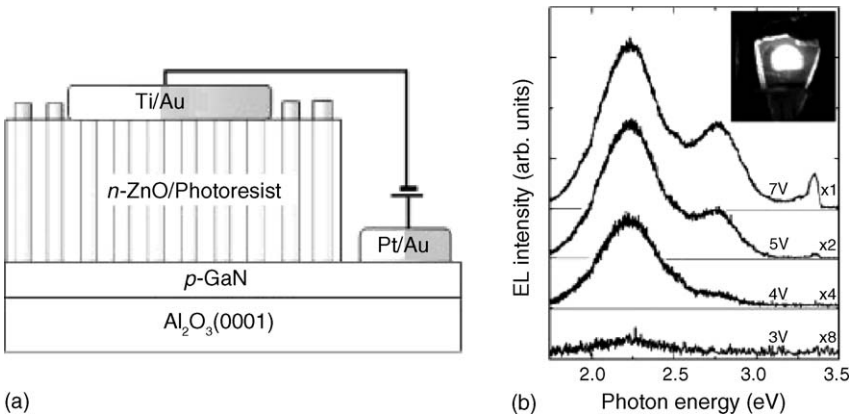


Fig. 22. (a) A schematic diagram of the *p*-GaN/*n*-ZnO nanorod heterojunction device. (b) Room-temperature EL spectra of a *p*-GaN/*n*-ZnO heterojunction device at different reverse-bias. The inset is a photograph of light emission at a 5 V reverse-bias (reprint permission from Ref. [71]).

### 4.2.3. *Polarization-dependent photodetector*

Besides UV emission and lasing, the photodetection property has been studied. Defect states related visible wavelength detection and polarized photodetection of ZnO nanowires [201,202], $SnO_2$ nanowires [7] and $In_2O_3$ nanowires have been observed [203]. Photoconductance is found to be proportional to $\cos^2\theta$, where $\theta$ is the angle between the polarization of incident light and long axis of the nanowire. It is a maximum when the electric field component of the incident light is polarized parallel to the nanowire long axis (Fig. 23a). Because nanowire diameter is much smaller than the light wavelength, electric field component of light normal to nanowire axis is effectively attenuated inside the nanowire. This interesting property can lead to promising application for Q1D polarization-dependent photodetectors and optically gated switches. In the photoconductivity measurements of ZnO nanowires, Fan et al. had found that the environment has a crucial effect on the photoresponse [202,204,205]. For example, surface chemical adsorption on the nanowires could significantly expedite the photocurrent relaxation time. As shown in Fig. 23b, the photocurrent relaxation time is around 8 s in air but hours in vacuum. This is because in air upon illumination, photogenerated holes discharge surface chemisorbed ions, while the photogenerated electrons

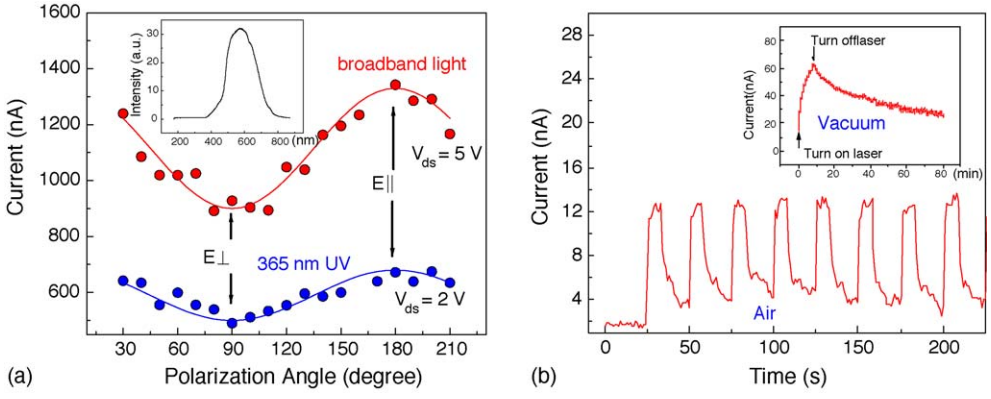


Fig. 23. (a) Polarized photodetection of both UV (365 nm) and visible light (spectrum shown in the inset) show that nanowire conductance is maximized when the electric field component of the incident light is polarized parallel to the nanowire axis. (b) Nanowire photoresponse to 633 nm laser in air compared to that in vacuum (inset) (reprint permission from Ref. [202]).

significantly increase the conductivity. When illumination is switched off, oxidizing gas (mainly $O_2$) molecules in air re-adsorb onto the surface and reduce the conductivity. The sensitivity to surface chemisorption is obviously important for chemical sensor application, which will be discussed in details in Section 4.4.

The existence of wide bandgap in metal oxides has been extensively exploited for blue-UV range optoelectronic applications. However, some metal oxides also exhibit infrared (IR) photodetection due to indirect bandgaps. For example, CdO has a small indirect bandgap of 0.55 eV. Liu et al. had shown photoconductivity measurements of CdO-based field-effect transistor with IR light illumination. The IR detection on/off ratio is about 8.6 at 1.2 K and the relaxation time constant is estimated to be 8.6 s.

### 4.2.4. Solar cell

The continuously increasing energy consumption has created an urgent need for alternative energy sources. The direct conversion of sunlight to electricity is doubtlessly a budget-effective and environment-friendly solution. Therefore, solar energy conversion device will play an important role in the blue print for future energy source. To employ nanotechnology into solar-cell system, semiconducting Q1D nanostructures have been implemented to function as the absorbing layers in photovoltaic solar cells [206]. It is predicted that such nanoscale absorber layer with discrete energy levels will improve the solar conversion efficiency. Other work have utilized nanowire array to replace the conventional nanoparticle film in dye-sensitized cells (DSC). Apart from the higher crystallinity and rapid carrier collection rate, the nanowire arrays are also advantageous for cell designs that could use non-standard electrolyte such as polymer gels or solid inorganic phases, in which the recombination rates are higher than the liquid electrolyte cell [207]. In these DSC systems, ZnO [207], $TiO_2$ [208] and CuO [209] nanowires had been used as the photo-anodes. Yang and his group bathed ZnO nanowire arrays into ruthenium based dye-sensitized cell, as shown in Fig. 24a. At a full Sun intensity of ~100 mW $cm^{-2}$, a conversion efficiency of 1.5% is reported with a nanowire filling factor of 0.37 [207]. Fig. 24b plots the current density versus bias voltage for two cells with different active areas. The small cell (with area 0.2 $cm^2$) shows higher short circuit current $J_{sc}$ and open circuit voltage $V_{oc}$ than the large cell (0.8 $cm^2$). The external quantum efficiency peaks at ~40% near the absorption maximum of the dye. Furthermore, a conversion efficiency up to 7% with denser filling factor of 0.70 based on $TiO_2$ nanorods was achieved by Jiu et al. [208]. Unlike other *n*-type oxide, CuO is a representative of *p*-type semiconducting oxides with a relative small bandgap energy of 1.2 eV.

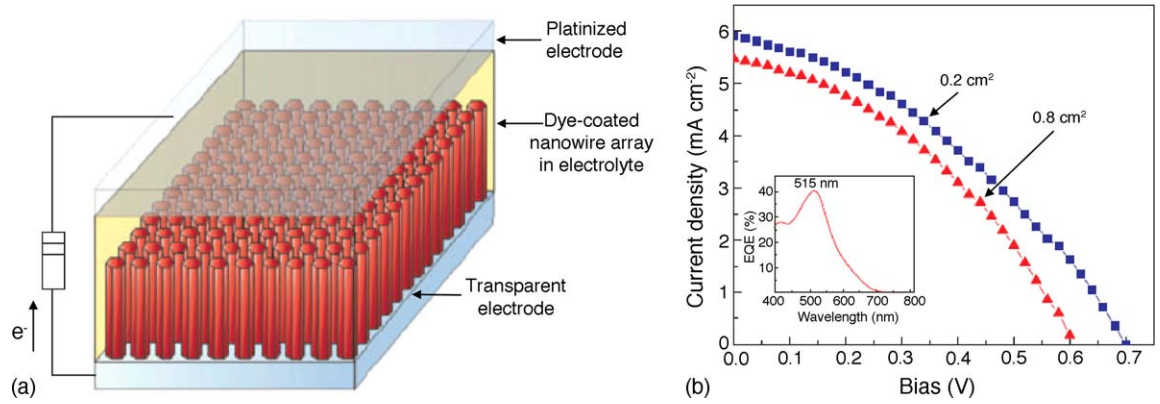


Fig. 24. (a) Schematic diagram of the ZnO nanowire array based dye-sensitized cell. Incident light is shone through the bottom transparent electrode. (b) Current density against voltage for two cells. The small cell shows a higher $V_{oc}$ and $J_{sc}$ than the large cell. Inset shows the external quantum efficiency vs. wavelength for the large cell (reprint permission from Ref. [207]).

This implies that CuO nanorods can act as the cathode in the dye-sensitized solar cell. Anandan et al. prepared CuO nanorods from solution phase on the Cu substrate as the cathode [209] and made the indium–tin oxide (ITO) conducting electrode coated with dye-absorbed $TiO_2$ nanoparticles as the anode. Such cell composed of ITO/$TiO_2$/dye/electrolyte/CuO nanorods/Cu was tested to yield a 0.29% conversion efficiency at 0.17 filling factor.

### 4.3. Resonator and cantilever

#### 4.3.1. Nano-resonator

Apart from theoretical modeling [210], characterizations of nanowire mechanical properties such as Young's modulus and resonant frequency are not easily performed due to the requirement of sophisticated instrumentation. As a pioneer work on the characterization of nanoscale mechanical property, Wang and his group presented the measurement of the bending modulus and piezoelectric property of nanostructures [211–215] using in situ TEM [212]. In this work, electric-field-induced excitation was applied to drive the harmonic resonances of Q1D structure. ZnO nanobelt [212], $SiO_2$/SiC composite [211], carbon nanotube [216] have been tested for the potential nano-resonator applications. On the other hand, other research groups had employed in situ SEM and electric field excitation techniques to characterize Young's modulus of β-$Ga_2O_3$ nanowire (Fig. 25a) [147] and amorphous $SiO_2$ nanowire [217]. In addition to electrically driven resonance, Ikuno et al. reported the observation of thermally driven mechanical deflection of $ZrO_x/SiO_x$ and $TiO_x/ZnO_x$ hybrid nanowires [218].

#### 4.3.2. Piezoelectric property

Researchers have developed several methods based on contact mode atomic force microscopy (AFM) to measure the elastic property of vertically standing ZnO nanowire [215] and piezoelectric property of ZnO nanobelt [213]. Elastic modulus of individual nanowire can be derived by simultaneously recording the topography and lateral force image while the AFM tip is scanning across the nanowire [215]. This principle originates from the dependence of the change of lateral force on nanowire bending. In addition, a piezoresponse force microscope (PFM) technique (Fig. 25b) evolved from AFM is used for studying ferroelectric and piezoelectric properties of Q1D metal oxide nanostructures including ZnO nanobelts [213], $KNbO_3$ (KN) nanorods [219], and $Pb(Zr_{0.53}Ti_{0.47})O_3$ (PZT) [220] nanowires. The PFM technique is based on detecting local mechanical deformation induced by an ac signal applied across the conductive AFM tip and the bottom electrode of the sample. In the recorded data, the amplitude of the piezoelectric response indicates the extent of the local

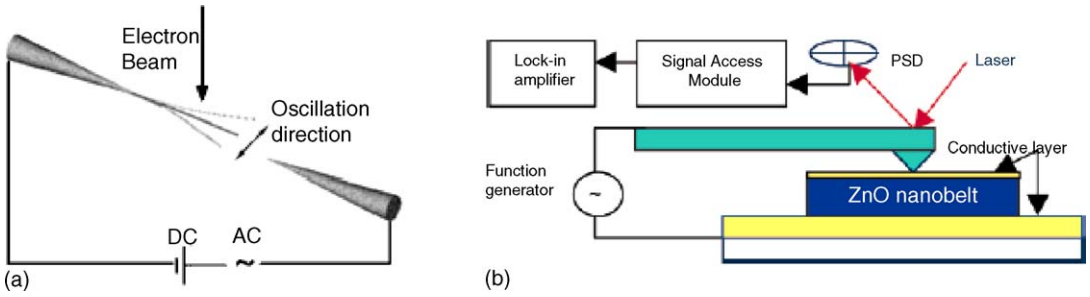


Fig. 25. (a) Schematic of the experimental set up showing the resonating $Ga_2O_3$ nanowire under the applied dc bias and ac driving signal (reprint permission from Ref. [147]). (b) Piezoresponse force microscope analysis is performed in contact mode with the addition of a function generator, a lock-in amplifier, and a signal access module (reprint permission from Ref. [213]).

piezoelectric phenomenon, and the phase related to the applied ac signal reveals the polarization direction of different ferroelectric domains.

### 4.4. Chemical sensor

Sensing behavior is the most important and well-known property of metal oxide materials. In addition to the sensitivity to light and pressure as mentioned in previous sections, metal oxides demonstrate high sensitivity to their chemical environment. With the capability of being operated in harsh environment, they surpass other chemical sensors in their sensitivity, reliability and durability. The advantage of using Q1D metal oxide nanostructures for chemical sensing is manifolds. With a large surface-to-volume ratio and a Debye length comparable to the nanowire radius, the electronic property of the nanowire is strongly influenced by surface processes, yielding superior sensitivity than their thin film counterpart. In order to achieve maximum sensitivity, thin film gas sensors are often operated at elevated temperature [221,222]. This indicates that a single sensing device needs to incorporate temperature control unit, which will certainly increase the complexity of sensor design and power consumption. Fortunately, metal oxide nanowire based gas sensors have demonstrated significantly higher sensitivity at room temperature. For example, room temperature $NO_2$ sensing with ZnO nanowire shows more than 50% conductance change under an exposure of 0.6 ppm $NO_2$ [223]; in contrast, $NO_2$ sensor made of doped ZnO thin film demonstrates less than 2% conductance change when exposed to an even higher concentration of $NO_2$ (1.5 ppm) [221]. This encouraging result manifests the potential of building room temperature operating highly sensitive gas sensors. In addition, metal oxide nanowires configured as field-effect transistors have demonstrated that a transverse electric field can effectively tune the sensing behavior of the system [223,224].

The sensing mechanism of metal oxides is mainly governed by the fact that the oxygen vacancies on the oxide surfaces are electrically and chemically active. In this case, two kinds of sensing responses have been observed. (1) Upon adsorption of charge accepting molecules, such as $NO_2$ and $O_2$, at the vacancy sites, electrons are withdrawn and effectively depleted from the conduction band, leading to a reduction of conductivity. (2) On the other hand, in an oxygen-rich environment, gas molecules such as CO and $H_2$, could react with the surface adsorbed oxygen and consequently release the captured electrons back to the channel, resulting in an increase in conductance. Conclusively, if one categorizes such redox sensing response into reducing and oxidizing, which manifests in an increase and a decrease in the channel conductance, the sensing responses can be represented using two examples:

Reducing response: $CO + O \rightarrow CO_2 + e^-$ (Ref. [225])
Oxidizing response: $NO + e^- \rightarrow NO^-$ (Ref. [226])

Selectivity has always been a major hurdle for solid state gas sensors. There have been a number of approaches developed to improve the selectivity of gas sensors, including doping metal impurities [227], using impedance measurement [228], modulating operating temperature [229], surface coating [230], etc. In the frame work of studying metal oxide nanowire field-effect sensors, it is discovered that the transverse electrical field induced by back gate can be utilized to distinguish different chemical gases [223,231]. Ultimate goal is to develop an ‘‘electronic nose’ system mimicking the mammalian olfactory system by assembling multi-component sensing modules integrated with signal processing and pattern recognition functions. This concept is illustrated in Fig. 26 [224].

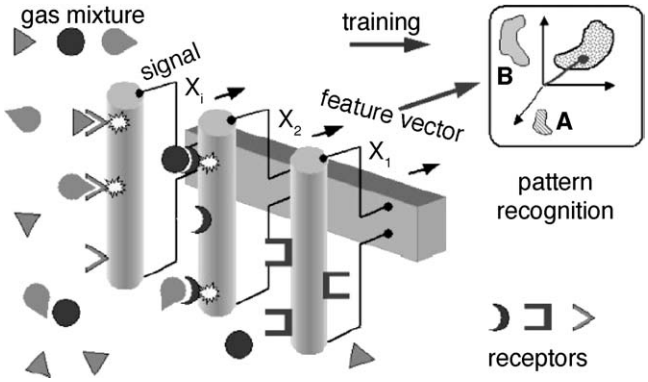


Fig. 26. A proposed nanowire-based "electronic nose". The nanowire surfaces may be functionalized with molecule-selective receptors. The operation is based on molecular selective bonding, signal transduction, and chemical detection through complex pattern recognition (reprint permission from Ref. [224]).

Bulk and thin film metal oxides have been used for sensing gas species such as CO, $CO_2$, $CH_4$, $C_2H_5OH$, $C_3H_8$, $H_2$, $H_2S$, $NH_3$, NO, $NO_2$, $O_2$, $O_3$, $SO_2$, acetone, humidity, etc. [232,233]. In the past few years, a surge of research effort focuses on the chemical sensing based on metal oxide nanowires, such as zinc oxide (ZnO), tin oxide ($SnO_2$), indium oxide ($In_2O_3$) aluminum oxide ($Al_2O_3$), gallium oxide ($Ga_2O_3$), tungsten oxide ($WO_3$), and vanadium oxide ($V_2O_5$). In the following sub-sections, the chemical sensing behaviors of some metal oxide nanowires to different chemical species will be described.

*4.4.1. ZnO*

**Oxygen ($O_2$), ozone ($O_3$) and nitrogen dioxide ($NO_2$)** are oxidizing gases that were found to be easily detected by ZnO. Pearton et al. proposed ZnO nanorod ozone sensors [234]. Because of the higher oxidizing ability of $O_3$, nanorods sensing response to ozone is pronounced in either $N_2$ or $O_2$ ambient.

Recently, Lu and coworkers reported $O_2$ and $NO_2$ oxidizing sensing with field-effect transistors constructed of individual ZnO nanowires [132,223]. The conductance of the nanowire FET decreases with the presence of $O_2$ and $NO_2$ (Fig. 27). In addition, it was observed that the sensitivity can be tuned by the back gate potential, i.e., above the gate threshold voltage of FET, sensitivity increases with decreasing gate voltage. This implies that the gate voltage can be used to adjust the sensitivity range. In addition, a gate-refreshing mechanism was proposed [223]. As demonstrated in Fig. 27, the conductance of

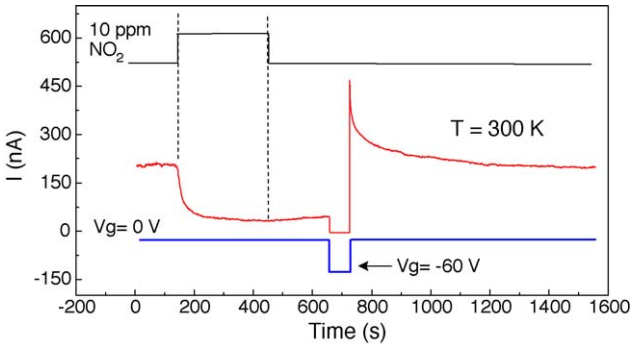


Fig. 27. Response of ZnO nanowire FET exposed to 10 ppm $NO_2$ gas then return to pure Ar. After applying a gate voltage pulse with 60 s duration, the conductance is turned off followed by a current surge. In about 4 min, the conductance recovers to the initial level (reprint permission from Ref. [223]).

nanowire can be electrically recovered by applying a negative gate voltage much larger than the threshold. The applied gate voltage weakens the bond and facilitates the desorption of the absorbed gas molecules, thus recovering the conductance of the sensor to the original level. This establishes an efficient method to refresh sensors at room temperature, as the refreshing procedure is normally performed by using UV illumination or thermal heating. Furthermore, it was shown that from the gate-refresh voltage and the temporal response of the electrical conductance, different chemical adsorbants can be distinguished. These results provide an exciting prospect of a novel hand-held sensor which utilizes the gate voltage as a knob to control sensitivity, refreshability as well as distinguishability.

**Ammonia ($NH_3$)** sensing shows temperature-dependent behavior. Fig. 28a illustrates oxidizing sensing response of a single ZnO nanowire to $NH_3$ at room temperature, manifested by a conductance decrease. However, at 500 K, the conductance shows an increase upon exposure to $NH_3$ (Fig. 28b). These phenomena are attributed to the fact that the chemical potentials of the nanowire and the ammonia adsorbants lie closely to each other, and the temperature induced chemical potential level shift results in the change of relative position of the chemical potentials, causing a reversal in the charge transfer direction [235]. Similar phenomena have also been observed in tungsten oxide $NH_3$ sensing, which will be discussed later [236].

**Carbon monoxide (CO)** is known as a reducing gas. CO sensing was carried out at 500 K in synthetic air (20% oxygen). Admittance of CO into the test chamber immediately increased the nanowire conductance. This is caused by the reaction between CO and the surface adsorbed $O_2$, which releases the electrons withdrawn by $O_2$ adsorption back to the conduction channel [235].

**Hydrogen ($H_2$)** detection and storage are drawing increasing attention due to the demand of solid oxide fuel cell which uses $H_2$ as a source. Pioneering works have been done by Pearton et al. on hydrogen sensing by utilizing treated and untreated ZnO nanorods. Pt [237], Pd [238]-coated and pristine ZnO nanorods have been examined, showing reducing response. It should be noted that hydrogen introduces a shallow donor state in ZnO which may also contribute to the conductance increase. Furthermore, surface functionalized nanorods have shown higher $H_2$ sensitivity down to 10 ppm and faster response time than pristine rods at room temperature.

**Hydrogen sulfide ($H_2S$)** sensing by using hydrothermally prepared ZnO nanorods has been tested [239,240]. Because of the low H–SH bond energy, $H_2S$ is easy to dissociate and can be readily detected at room temperature, showing a conductance increase. Wang et al. [240] has demonstrated the sensitivity down to 50 ppb of $H_2S$ at room temperature.

**Ethanol ($C_2H_5OH$)** is a commonly used flammable chemical. Compared to $H_2S$, because of the moderately higher bond energies in $C_2H_5OH$, reducing sensing response is only pronounced at

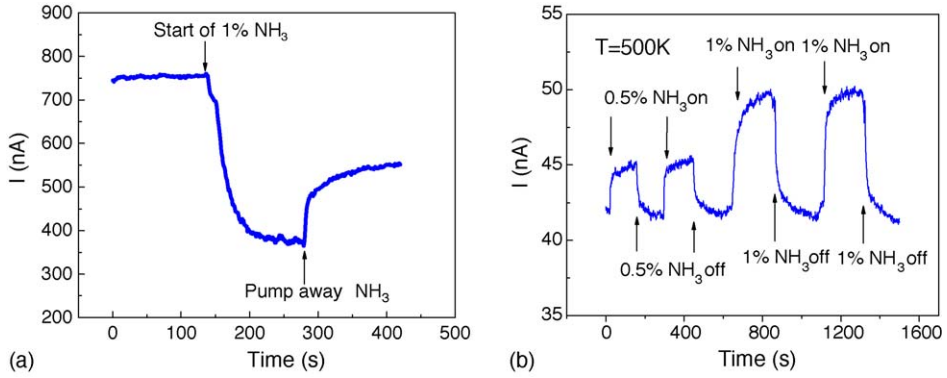


Fig. 28. (a) ZnO nanowire conductance decreases in the presence of $NH_3$ at room temperature (b) Conductance increases when exposed to $NH_3$ at 500 K (reprint permission from Ref. [235]).

elevated temperature [240]. Wan et al. fabricated ZnO nanowire ethanol sensors using micro-electromechanical system (MEMS) technology [241]. In that work, nanowires were placed between Pt interdigitating electrodes. Under an operation temperature of 300 °C, the resistance of nanowires significantly decreased upon exposure to ethanol vapor.

**Humidity ($H_2O$)** sensing has been tested on Cd-doped ZnO nanowires [255]. It is suggested that water molecules are dissociated at the oxygen vacancies, thus providing protons as charge carriers for the hopping transport in low humidity environment. In contrast, at high humidity, water condensed on the nanowire surface aids the electrolytic conduction of protonic transport and further increases the conductance.

### *4.4.2. $SnO_2$*

Tin oxide has been intensively studied as chemical sensor. In a number of reports, $SnO_2$ nanowire [225] and nanobelt [242] sensors were used to detect $O_2$ [225,243], $NO_2$ [226,242], CO [225,226,242], ethanol [242,244,245], and $H_2$ [243]. As in ZnO sensing studies, $SnO_2$ is able to detect both oxidizing and reducing gas governing by the same mechanism. Instead of employing pristine oxide materials, new techniques have been inspired. Kolmakov et al. proposed an enhanced $SnO_2$ nanowire gas sensor for $H_2$ and $O_2$ [246]. They deposited functional Pd particles onto the nanostructure surface as catalysts. These Pd particles modify the surface and the oxygen adsorption kinetics. It is well known that Pd is a good oxygen dissociation catalyst. These nanoparticles assist the dissociation of $O_2$ molecules, thus increase the number of oxygen ions that can be adsorbed. This effect results in a more pronounced conductance change and a faster response time. The schematic of Pd-assisted adsorption process is illustrated in Fig. 29a. There are three major steps: (1) ionosorption of oxygen at defect sites of the pristine nanowire surface; (2) molecular oxygen dissociation on Pd nanoparticles followed by spillover of the atomic species onto the oxide surface; (3) capturing of weakly adsorbed molecular oxygen by Pd nanoparticles. These oxygen molecules have diffused along the tin oxide surface to the Pd nanoparticle vicinity (followed by process 2) where $R_S$ in Fig. 29b represents the effective radius of the spillover zone, and $R_C$ represents the radius of the collection region. Fig. 29c shows different sensing response of functionalized and pristine $SnO_2$ nanostructures to oxygen and hydrogen.

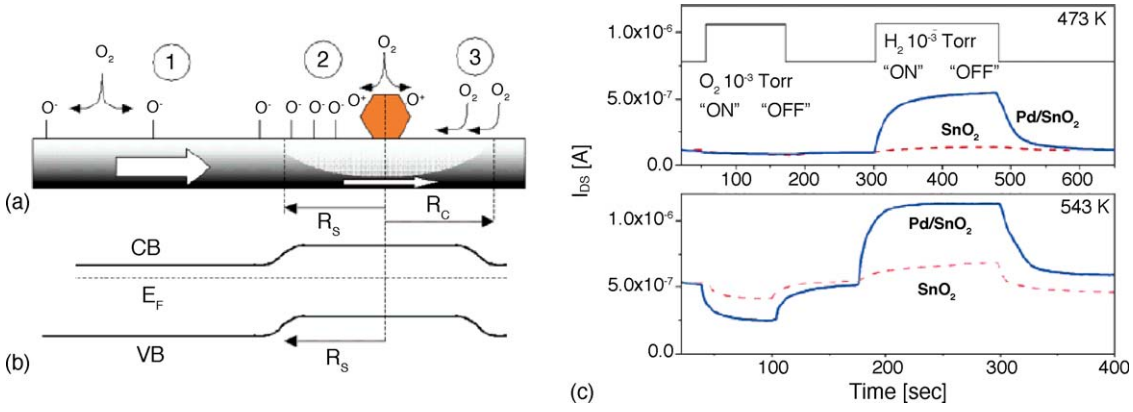


Fig. 29. (a) Schematic depiction of the three major processes taking place on $SnO_2$ nanostructure surface. $R_s$ is the effective radius of the spillover zone, and $R_c$ is the radius of the collection zone. (b) Band diagram of the pristine $SnO_2$ nanostructure and in the vicinity (and beneath) of a Pd nanoparticle. The radius of the depletion region is determined by the radius of the spillover zone. (c) Response of a pristine (dashed line) and Pd-functionalized (solid line) nanostructure to sequential oxygen and hydrogen pulses at 473 K (top panel) and 543 K (bottom) (reprint permission from Ref. [246]).

In addition, sensors made from $SnO_2$ nanobelts have been assembled for sensitive and stable detection of nerve gases [247]. A 10 nm thick single-crystal nanobelt of $SnO_2$ is sandwiched between two Pt electrodes. Since sensitivity is enhanced by heating, a MEMS fabrication of a suspended, thermally isolated SiN membrane element was employed to facilitate heating to 500 °C. Conductance was found to increase 5% on exposure to 78 ppb in air of dimethyl methylphosphonate (DMMP) molecules, a non-toxic stimulant nerve gas.

#### 4.4.3. $In_2O_3$

Several studies on $In_2O_3$ nanowire sensing of ethanol, $NH_3$, $NO_2$ have been reported. Ethanol sensor using $In_2O_3$ nanowires prepared by carbonthermal synthesis was fabricated by Chu et al. [248]. It shows an increase in channel conductance. On the other hand, Li et al. have investigated oxidizing gas sensing of $NO_2$ and $NH_3$ [249]. In this work, detection of $NO_2$ down to 5 ppb levels at room temperature has been achieved by using a mesh of multiple-wires [250]. As mentioned previously, $NH_3$ demonstrates oxidizing sensing at room temperature and reducing sensing at high temperature. Similar to this temperature-dependent change in the sensing response, Li et al. manipulated the carrier concentration and thus the chemical potential by carefully adjusting oxygen partial pressure during the CVD growth, and observed the reverse sensing behavior [108], i.e., lower (higher) carrier concentration corresponding to lower (higher) chemical potential yielding reducing (oxidizing) sensing performance.

#### 4.4.4. $V_2O_5$

The drawback of metal oxide sensing is a lack of selectivity. Interestingly, vanadium pentoxide nanobelts have proven to be highly selective in the sensing of ethanol vapor [251]. $V_2O_5$ nanoebelts grown by hydrothermal method were measured in temperature ranging from 150 °C to 400 °C and showed remarkably stable reducing sensing response. To determine the selectivity, potential interfering species, such as CO and $H_2$ reducing gases were introduced and showed negligible affect on the conductance response. In addition, $V_2O_5$ is found to be highly sensitive to organic amine due to its good affinity to amine species. Raible et al. used $V_2O_5$ nanowires as vapor sensors to detect 1-butylamine [252]. They demonstrate high sensitivity with detection limit down to 30 ppb, which is significantly below the sensitivity of the human olfactory system. They also show negligible response to background toluene and 1-propanol vapors.

#### 4.4.5. $WO_x$

Non-stoichiometric tungsten oxide ($WO_x$) prepared with solution based methods was proposed to detect $NO_2$ [236,253,254], ethanol and $NH_3$ [236]. In the $NH_3$ sensing study, the reverse of sensing response was observed at different temperatures. Kim et al. reported that the *n*-type $WO_{2.72}$ nanowire sensor encountered a resistance decrease at temperature higher than 150 °C, and an increase under operating temperature below 70 °C. This echoes with the observation on ZnO nanowire's sensing response to $NH_3$, showing that the temperature induced chemical potential shift in the metal oxide with respect to that of target gas governs the direction of charge transfer. This renders an ammonia-selective sensor by monitoring the temperature dependence of the sensing response.

## 5. Conclusion—present achievements and future challenges

This article provides an up-to-date review of the current achievements on the investigation of Q1D metal oxide materials, ranging from synthesis, characterizations, and device applications.

Due to the tremendous research effort, this article is unable to cover all the exciting work reported in this field.

Synthesis of Q1D structures has been well-developed and an assortment of metal oxide nanowires, nanoneedles, nanobelts, and nanotubes are successfully obtained. Such wealth of Q1D materials has provided a playground for fundamental studies as well as technological developments. In fact, immense effort has been devoted in device applications utilizing single crystalline Q1D structures as nano laser, field-effect transistor, cantilever, and chemical sensor. As a whole, the research based on individual metal oxide nanostructures has been successful, and the alignment of these nanostructures towards device integration has also achieved considerable progress. These studies pave the way for the future applications of the Q1D metal oxides in integrated nanoelectronics and sensing devices.

These fascinating achievements inspire more research effort to address the challenges that remains. One key issue is the growth of *p*-type ZnO nanostructures and fabrication of intra-nanowire *p–n* junctions. Although various techniques have been developed to achieve *p*-type ZnO thin film, *p*-type ZnO Q1D system is still difficult to achieve. To realize *p*-doping will significantly advance the device application of ZnO Q1D structures.

Another critical issue is the selective gas detection based on Q1D metal oxides. As known, metal oxide Q1D system demonstrates superior sensitivity to various gases. However, selectivity has always been an obstacle for practical applications. Promising solutions lie in surface coating with chemical selective membrane, surface modification by specific functional groups, or combining multi-component sensing modules coupled with signal processing functions, acting as an ''electronic nose'' to differentiate minute quantities in a complex environment.

Last but not the least, there is much new science awaits to elucidate, especially the quantum behaviors that are expected to dominate as the size of Q1D metal oxides continues to reduce. The quantum confinement will provide the means to study and manipulate individual quantum states of electrons, spins and phonons. The development of devices based on the unique quantum properties will lead a great leap forward and promote a wide range of technological advancement.

## Acknowledgments

Paichun Chang and Zhiyong Fan contributed equally to the manuscript. The authors thank D. Wang, C.J. Chien, and D. Niu for literature search assistance. And the work is made possible by NSF grants ECS-0306735 and EEC-0210120.

## References

[1] G.E. Moore, Cramming more components onto integrated circuits, Proc. IEEE 86 (1998) 82 (Reprinted from Electronics, pp. 114–117, April 19, 1965).
[2] P.S. Peercy, The drive to miniaturization, Nature 406 (2000) 1023.
[3] E. Regis, Nano: The Emerging Science of Nanotechnology—Remaking the World-Molecule by Molecule, Little Brown and Company, Boston, 1995.
[4] C.N.R. Rao, F.L. Deepak, G. Gundiah, A. Govindaraj, Inorganic nanowires, Prog. Solid State Chem. 31 (2003) 5.
[5] Z.R. Dai, Z.W. Pan, Z.L. Wang, Novel nanostructures of functional oxides synthesized by thermal evaporation, Adv. Funct. Mater. 13 (2003) 9.
[6] D.H. Zhang, C. Li, S. Han, et al., Electronic transport studies of single-crystalline $In_2O_3$ nanowires, Appl. Phys. Lett. 82 (2003) 112.
[7] Z.Q. Liu, D.H. Zhang, S. Han, et al., Laser ablation synthesis and electron transport studies of tin oxide nanowires, Adv. Mater. 15 (2003) 1754.

[8] X. Liu, C. Li, S. Han, J. Han, C.W. Zhou, Synthesis and electronic transport studies of CdO nanoneedles, Appl. Phys. Lett. 82 (2003) 1950.
[9] W.I. Park, D.H. Kim, S.W. Jung, G.C. Yi, Metalorganic vapor-phase epitaxial growth of vertically well-aligned ZnO nanorods, Appl. Phys. Lett. 80 (2002) 4232.
[10] G. Malandrino, S.T. Finocchiaro, R. Lo Nigro, C. Bongiorno, C. Spinella, I.L. Fragala, Free-standing copper(II) oxide nanotube arrays through an MOCVD template process, Chem. Mater. 16 (2004) 5559.
[11] H.W. Kim, N.H. Kim, Synthesis of beta-$Ga_2O_3$ nanowires by an MOCVD approach, Appl. Phys. A Mater. Sci. Process. 81 (2005) 763.
[12] R.S. Wagner, W.C. Ellis, Vapor–liquid–solid mechanism of single crystal growth (new method growth catalysis from impurity whisker epitaxial + large crystals Si E), Appl. Phys. Lett. 4 (1964) 89.
[13] R.S. Wagner, W.C. Ellis, S.M. Arnold, K.A. Jackson, Study of filamentary growth of silicon crystals from vapor, J. Appl. Phys. 35 (1964) 2993.
[14] X. Liu, X.H. Wu, H. Cao, R.P.H. Chang, Growth mechanism and properties of ZnO nanorods synthesized by plasma-enhanced chemical vapor deposition, J. Appl. Phys. 95 (2004) 3141.
[15] Y.Y. Wu, P.D. Yang, Direct observation of vapor–liquid–solid nanowire growth, J. Am. Chem. Soc. 123 (2001) 3165.
[16] S.Y. Bae, H.W. Seo, J.H. Park, Vertically aligned sulfur-doped ZnO nanowires synthesized via chemical vapor deposition, J. Phys. Chem. B 108 (2004) 5206.
[17] Y.J. Chen, J.B. Li, Y.S. Han, X.Z. Yang, J.H. Dai, The effect of Mg vapor source on the formation of MgO whiskers and sheets, J. Cryst. Growth 245 (2002) 163.
[18] J.M. Wu, H.C. Shih, W.T. Wu, Y.K. Tseng, I.C. Chen, Thermal evaporation growth and the luminescence property of $TiO_2$ nanowires, J. Cryst. Growth 281 (2005) 384.
[19] Z.R. Dai, J.L. Gole, J.D. Stout, Z.L. Wang, Tin oxide nanowires, nanoribbons, and nanotubes, J. Phys. Chem. B 106 (2002) 1274.
[20] L. Dai, X.L. Chen, J.K. Jian, M. He, T. Zhou, B.Q. Hu, Fabrication and characterization of $In_2O_3$ nanowires, Appl. Phys. A Mater. Sci. Process. 75 (2002) 687.
[21] P.C. Chang, Z.Y. Fan, W.Y. Tseng, A. Rajagopal, J.G. Lu, beta-$Ga_2O_3$ nanowires: synthesis, characterization, and *p*-channel field-effect transistor, Appl. Phys. Lett. 87 (2005) 222102.
[22] P.D. Yang, H.Q. Yan, S. Mao, et al., Controlled growth of ZnO nanowires and their optical properties, Adv. Funct. Mater. 12 (2002) 323.
[23] X.D. Wang, C.J. Summers, Z.L. Wang, Large-scale hexagonal-patterned growth of aligned ZnO nanorods for nano-optoelectronics and nanosensor arrays, Nano Lett. 4 (2004) 423.
[24] Y.K. Tseng, I.N. Lin, K.S. Liu, T.S. Lin, I.C. Chen, Low-temperature growth of ZnO nanowires, J. Mater. Res. 18 (2003) 714.
[25] H.B. Huang, S.G. Yang, J.F. Gong, et al., Controllable assembly of aligned ZnO nanowires/belts arrays, J. Phys. Chem. B 109 (2005) 20746.
[26] Q. Zhao, X. Xu, H. Zhang, Y. Chen, J. Xu, D. Yu, Catalyst-free growth of single-crystalline alumina nanowire arrays, Appl. Phys. A Mater. Sci. Process. 79 (2004) 1721.
[27] A. Umar, S.H. Kim, Y.S. Lee, K.S. Nahm, Y.B. Hahn, Catalyst-free large-quantity synthesis of ZnO nanorods by a vapor–solid growth mechanism: structural and optical properties, J. Cryst. Growth 282 (2005) 131.
[28] A. Sekar, S.H. Kim, A. Umar, Y.B. Hahn, Catalyst-free synthesis of ZnO nanowires on Si by oxidation of Zn powders, J. Cryst. Growth 277 (2005) 471.
[29] Y. Sun, G.M. Fuge, M.N.R. Ashfold, Growth mechanisms for ZnO nanorods formed by pulsed laser deposition, Superlattices Microstruct. 39 (2006) 33.
[30] N. Cabrera, W.K. Burton, Crystal growth and surface structure. 2, Discuss. Faraday Soc. (1949) 40.
[31] G.W. Sears, A mechanism of whisker growth, Acta Metallurgica 3 (1955) 367.
[32] J.M. Blakely, K.A. Jackson, Growth of crystal whiskers, J. Chem. Phys. 37 (1962) 428.
[33] J.C. Hulteen, C.R. Martin, A general template-based method for the preparation of nanomaterials, J. Mater. Chem. 7 (1997) 1075.
[34] D.S. Xue, L.Y. Zhang, A.B. Gui, X.F. Xu, $Fe_3O_4$ nanowire arrays synthesized in AAO templates, Appl. Phys. A Mater. Sci. Process. 80 (2005) 439.
[35] M.J. Zheng, L.D. Zhang, G.H. Li, W.Z. Shen, Fabrication and optical properties of large-scale uniform zinc oxide nanowire arrays by one-step electrochemical deposition technique, Chem. Phys. Lett. 363 (2002) 123.
[36] K.Y. Shi, B.F. Xin, Y.J. Chi, H.G. Fu, Assembling porous $Fe_2O_3$ nanowire arrays by electrochemical deposition in mesoporous silica SBA-16 films, Acta Chim. Sin. 62 (2004) 1859.

[37] X.M. Liu, Y.C. Zhou, Electrochemical deposition and characterization of $Cu_2O$ nanowires, Appl. Phys. A Mater. Sci. Process. 81 (2005) 685.
[38] T.S. Mintz, Y.V. Bhargava, S.A. Thorne, et al., Electrochemical synthesis of functionalized nickel oxide nanowires, Electrochem. Solid State Lett. 8 (2005) D26.
[39] Y.H. Chen, X.T. Zhang, Z.H. Xue, Z.L. Du, T.J. Li, Preparation of $SnO_2$ nanowires by AC electrodeposition in anodic alumina template and its deposition conditions, J. Inorg. Mater. 20 (2005) 59.
[40] Y. Li, G.S. Cheng, L.D. Zhang, Fabrication of highly ordered ZnO nanowire arrays in anodic alumina membranes, J. Mater. Res. 15 (2000) 2305.
[41] Y.W. Chen, Y.C. Liu, S.X. Lu, et al., Optical properties of ZnO and ZnO: In nanorods assembled by sol–gel method, J. Chem. Phys. 123 (2005) 134701.
[42] X.Y. Wang, X.Y. Wang, W.G. Huang, P.J. Sebastian, S. Gamboa, Sol–gel template synthesis of highly ordered $MnO_2$ nanowire arrays, J. Power Sources 140 (2005) 211.
[43] H. Xu, D.H. Qin, Z. Yang, H.L. Li, Fabrication and characterization of highly ordered zirconia nanowire arrays by sol–gel template method, Mater. Chem. Phys. 80 (2003) 524.
[44] M. Zhang, Y. Bando, K. Wada, Sol–gel template preparation of $TiO_2$ nanotubes and nanorods, J. Mater. Sci. Lett. 20 (2001) 167.
[45] Y.K. Zhou, H.L. Li, Sol–gel template synthesis and structural properties of a highly ordered $LiNi_{0.5}Mn_{0.5}O_2$ nanowire array, J. Mater. Chem. 12 (2002) 681.
[46] Z. Yang, Y. Huang, B. Dong, H.L. Li, Fabrication and structural properties of $LaFeO_3$ nanowires by an ethanol–ammonia-based sol–gel template route, Appl. Phys. A Mater. Sci. Process. 81 (2005) 453.
[47] C.K. Xu, G.D. Xu, Y.K. Liu, G.H. Wang, A simple and novel route for the preparation of ZnO nanorods, Solid State Commun. 122 (2002) 175.
[48] C.K. Xu, X.L. Zhao, S. Liu, G.H. Wang, Large-scale synthesis of rutile $SnO_2$ nanorods, Solid State Commun. 125 (2003) 301.
[49] C.K. Xu, G.D. Xu, G.H. Wang, Preparation and characterization of NiO nanorods by thermal decomposition of $NiC_2O_4$ precursor, J. Mater. Sci. 38 (2003) 779.
[50] Y.L. Cao, D.Z. Jia, L. Liu, J.M. Luo, Rapid synthesis of lead oxide nanorods by one-step solid-state chemical reaction at room temperature, Chin. J. Chem. 22 (2004) 1288.
[51] J.H. Liang, C. Peng, X. Wang, et al., Chromate nanorods/nanobelts: general synthesis, characterization, and properties, Inorg. Chem. 44 (2005) 9405.
[52] A. Vantomme, Z.Y. Yuan, G.H. Du, B.L. Su, Surfactant-assisted large-scale preparation of crystalline $CeO_2$ nanorods, Langmuir 21 (2005) 1132.
[53] L.H. Thompson, L.K. Doraiswamy, Sonochemistry: science and engineering, Ind. Eng. Chem. Res. 38 (1999) 1215.
[54] R.V. Kumar, Y. Koltypin, X.N. Xu, Y. Yeshurun, A. Gedanken, I. Felner, Fabrication of magnetite nanorods by ultrasound irradiation, J. Appl. Phys. 89 (2001) 6324.
[55] X.L. Hu, Y.J. Zhu, S.W. Wing, Sonochemical and microwave-assisted synthesis of linked single-crystalline ZnO rods, Mater. Chem. Phys. 88 (2004) 421.
[56] T. Gao, Q.H. Li, T.H. Wang, Sonochemical synthesis, optical properties, and electrical properties of core/shell-type ZnO nanorod/CdS nanoparticle composites, Chem. Mater. 17 (2005) 887.
[57] V.G. Pol, O. Palchik, A. Gedanken, I. Felner, Synthesis of europium oxide nanorods by ultrasound irradiation, J. Phys. Chem. B 106 (2002) 9737.
[58] J.J. Miao, H. Wang, Y.R. Li, J.M. Zhu, J.J. Zhu, Ultrasonic-induced synthesis of $CeO_2$ nanotubes, J. Cryst. Growth 281 (2005) 525.
[59] B. Liu, H.C. Zeng, Hydrothermal synthesis of ZnO nanorods in the diameter regime of 50 nm, J. Am. Chem. Soc. 125 (2003) 4430.
[60] J.M. Wang, L. Gao, Wet chemical synthesis of ultralong and straight single-crystalline ZnO nanowires and their excellent UV emission properties, J. Mater. Chem. 13 (2003) 2551.
[61] M. Guo, P. Diao, S.M. Cai, Hydrothermal growth of well-aligned ZnO nanorod arrays: dependence of morphology and alignment ordering upon preparing conditions, J. Solid State Chem. 178 (2005) 1864.
[62] M.H. Cao, Y.H. Wang, C.X. Guo, Y.J. Qi, C.W. Hu, E.B. Wang, A simple route towards CuO nanowires and nanorods, J. Nanosci. Nanotechnol. 4 (2004) 824.
[63] C. Chen, Z.B. Zhuang, Q. Peng, Synthesis and characterization of cadmium orthosilicate nanowires, Chem. J. Chin. Univ. Chin. 26 (2005) 1220.
[64] J. Zhang, Z.G. Liu, C.K. Lin, J. Lin, A simple method to synthesize beta-$Ga_2O_3$ nanorods and their photoluminescence properties, J. Cryst. Growth 280 (2005) 99.

[65] D.S. Zheng, S.X. Sun, W.L. Fan, et al., One-step preparation of single-crystalline beta-$MnO_2$ nanotubes, J. Phys. Chem. B 109 (2005) 16439.
[66] D.L. Zhu, H. Zhu, Y.H. Zhang, Microstructure and magnetization of single-crystal perovskite manganites nanowires prepared by hydrothermal method, J. Cryst. Growth 249 (2003) 172.
[67] K.B. Zhou, X. Wang, X.M. Sun, Q. Peng, Y.D. Li, Enhanced catalytic activity of ceria nanorods from well-defined reactive crystal planes, J. Catal. 229 (2005) 206.
[68] Z.Y. Yuan, B.L. Su, Titanium oxide nanotubes, nanofibers and nanowires, Colloids Surf. A Physicochem. Eng. Aspects 241 (2004) 173.
[69] T. Martensson, P. Carlberg, M. Borgstrom, L. Montelius, W. Seifert, L. Samuelson, Nanowire arrays defined by nanoimprint lithography, Nano Lett. 4 (2004) 699.
[70] X.C. Jiang, T. Herricks, Y.N. Xia, CuO nanowires can be synthesized by heating copper substrates in air, Nano Lett. 2 (2002) 1333.
[71] W.I. Park, G.C. Yi, Electroluminescence in *n*-ZnO nanorod arrays vertically grown on *p*-GaN, Adv. Mater. 16 (2004) 87.
[72] H.J. Fan, F. Bertram, A. Dadgar, J. Christen, A. Krost, M. Zacharias, Self-assembly of ZnO nanowires and the spatial resolved characterization of their luminescence, Nanotechnology 15 (2004) 1401.
[73] Y.K. Tseng, C.T. Chia, C.Y. Tsay, et al., Growth of epitaxial needle like ZnO nanowires on GaN films, J. Electrochem. Soc. 152 (2005) G95.
[74] H.T. Ng, J. Han, T. Yamada, P. Nguyen, Y.P. Chen, M. Meyyappan, Single crystal nanowire vertical surround-gate field-effect transistor, Nano Lett. 4 (2004) 1247.
[75] C.Y. Geng, Y. Jiang, Y. Yao, et al., Well-aligned ZnO nanowire arrays fabricated on silicon substrates, Adv. Funct. Mater. 14 (2004) 589.
[76] Y. Zhang, H.B. Jia, R.M. Wang, et al., Low-temperature growth and Raman scattering study of vertically aligned ZnO nanowires on Si substrate, Appl. Phys. Lett. 83 (2003) 4631.
[77] J. Park, H.H. Choi, K. Siebein, R.K. Singh, Two-step evaporation process for formation of aligned zinc oxide nanowires, J. Cryst. Growth 258 (2003) 342.
[78] S.Y. Li, P. Lin, C.Y. Lee, M.S. Ho, T.Y. Tseng, Fabrication of vertical ZnO nanowires on silicon(1 0 0) with epitaxial ZnO buffer layer, J. Nanosci. Nanotechnol. 4 (2004) 968.
[79] J.C. Johnson, K.P. Knutsen, H.Q. Yan, et al., Ultrafast carrier dynamics in single ZnO nanowire and nanoribbon lasers, Nano Lett. 4 (2004) 197.
[80] Z.Y. Fan, J.G. Lu, Unpublished works, 2006.
[81] C.H. Liu, W.C. Yiu, F.C.K. Au, J.X. Ding, C.S. Lee, S.T. Lee, Electrical properties of zinc oxide nanowires and intramolecular *p–n* junctions, Appl. Phys. Lett. 83 (2003) 3168.
[82] O. Englander, D. Christensen, L.W. Lin, Local synthesis of silicon nanowires and carbon nanotubes on microbridges, Appl. Phys. Lett. 82 (2003) 4797.
[83] A. Ural, Y.M. Li, H.J. Dai, Electric-field-aligned growth of single-walled carbon nanotubes on surfaces, Appl. Phys. Lett. 81 (2002) 3464.
[84] S. Dittmer, J. Svensson, E.E.B. Campbell, Electric field aligned growth of single-walled carbon nanotubes, Curr. Appl. Phys. 4 (2004) 595.
[85] O. Harnack, C. Pacholski, H. Weller, A. Yasuda, J.M. Wessels, Rectifying behavior of electrically aligned ZnO nanorods, Nano Lett. 3 (2003) 1097.
[86] S. Kumar, S. Rajaraman, R.A. Gerhardt, Z.L. Wang, P.J. Hesketh, Tin oxide nanosensor fabrication, using AC dielectrophoretic manipulation of nanobelts, Electrochim. Acta 51 (2005) 943.
[87] C.G. Van de Walle, S. Limpijumnong, J. Neugebauer, First-principles studies of beryllium doping of GaN, Phys. Rev. B 6324 (2001) 245205.
[88] S.F.J. Cox, E.A. Davis, S.P. Cottrell, et al., Experimental confirmation of the predicted shallow donor hydrogen state in zinc oxide, Phys. Rev. Lett. 86 (2001) 2601.
[89] T. Yamamoto, H. Katayama-Yoshida, Solution using a codoping method to unipolarity for the fabrication of *p*-type ZnO, Jpn. J. Appl. Phys. Part 2 Lett. 38 (1999) L166.
[90] J.G. Lu, L.P. Zhu, Z.Z. Ye, et al., Reproducibility and stability of N–Al codoped *p*-type ZnO thin films, J. Mater. Sci. 41 (2006) 467.
[91] J. Zhong, S. Muthukumar, Y. Chen, et al., Ga-doped ZnO single-crystal nanotips grown on fused silica by metal organic chemical vapor deposition, Appl. Phys. Lett. 83 (2003) 3401.
[92] S.Y. Bae, C.W. Na, J.H. Kang, J. Park, Comparative structure and optical properties of Ga-, In-, and Sn-doped ZnO nanowires synthesized via thermal evaporation, J. Phys. Chem. B 109 (2005) 2526.

[93] S.Y. Li, P. Lin, C.Y. Lee, T.Y. Tseng, C.J. Huang, Effect of Sn dopant on the properties of ZnO nanowires, J. Phys. D Appl. Phys. 37 (2004) 2274.
[94] D.K. Hwang, H.S. Kim, J.H. Lim, et al., Study of the photoluminescence of phosphorus-doped *p*-type ZnO thin films grown by radio-frequency magnetron sputtering, Appl. Phys. Lett. 86 (2005) 151917.
[95] W. Lee, M.C. Jeong, S.W. Joo, J.M. Myoung, Arsenic doping of ZnO nanowires by post-annealing treatment, Nanotechnology 16 (2005) 764.
[96] W. Lee, M.C. Jeong, J.M. Myoung, Optical characteristics of arsenic-doped ZnO nanowires, Appl. Phys. Lett. 85 (2004) 6167.
[97] D.W. Zeng, C.S. Xie, B.L. Zhu, et al., Controlled growth of ZnO nanomaterials via doping Sb, J. Cryst. Growth 266 (2004) 511.
[98] G.Z. Shen, J.H. Cho, J.K. Yoo, G.C. Yi, C.J. Lee, Synthesis and optical properties of S-doped ZnO nanostructures: nanonails and nanowires, J. Phys. Chem. B 109 (2005) 5491.
[99] J.B. Cui, U.J. Gibson, Electrodeposition and room temperature ferromagnetic anisotropy of Co and Ni-doped ZnO nanowire arrays, Appl. Phys. Lett. 87 (2005) 133108.
[100] C.X. Xu, X.W. Sun, Z.L. Dong, M.B. Yu, Y.Z. Xiong, J.S. Chen, Magnetic nanobelts of iron-doped zinc oxide, Appl. Phys. Lett. 86 (2005) 173110.
[101] D.A. Schwartz, K.R. Kittilstved, D.R. Gamelin, Above-room-temperature ferromagnetic $Ni^{2+}$-doped ZnO thin films prepared from colloidal diluted magnetic semiconductor quantum dots, Appl. Phys. Lett. 85 (2004) 1395.
[102] C. Ronning, P.X. Gao, Y. Ding, Z.L. Wang, D. Schwen, Manganese-doped ZnO nanobelts for spintronics, Appl. Phys. Lett. 84 (2004) 783.
[103] P.C. Chang, Z.Y. Fan, D.W. Wang, et al., ZnO nanowires synthesized by vapor trapping CVD method, Chem. Mater. 16 (2004) 5133.
[104] P. Sharma, A. Gupta, K.V. Rao, et al., Ferromagnetism above room temperature in bulk and transparent thin films of Mn-doped ZnO, Nat. Mater. 2 (2003) 673.
[105] Y.Q. Chang, D.B. Wang, X.H. Luo, et al., Synthesis, optical, and magnetic properties of diluted magnetic semiconductor $Zn_{1-x}Mn_xO$ nanowires via vapor phase growth, Appl. Phys. Lett. 83 (2003) 4020.
[106] Z.Y. Fan, X.G. Wen, S.H. Yang, J.G. Lu, Controlled *p*- and *n*-type doping of $Fe_2O_3$ nanobelt field effect transistors, Appl. Phys. Lett. 87 (2005) 013113.
[107] H.J. Chun, Y.S. Choi, S.Y. Bae, H.C. Choi, J. Park, Single-crystalline gallium-doped indium oxide nanowires, Appl. Phys. Lett. 85 (2004) 461.
[108] C. Li, D.H. Zhang, B. Lei, S. Han, X.L. Liu, C.W. Zhou, Surface treatment and doping dependence of $In_2O_3$ nanowires as ammonia sensors, J. Phys. Chem. B 107 (2003) 12451.
[109] D.J. Zhang, C. Li, X.L. Liu, S. Han, T. Tang, C.W. Zhou, Doping dependent $NH_3$ sensing of indium oxide nanowires, Appl. Phys. Lett. 83 (2003) 1845.
[110] X.S. Peng, G.W. Meng, X.F. Wang, et al., Synthesis of oxygen-deficient indium–tin–oxide (ITO) nanofibers, Chem. Mater. 14 (2002) 4490.
[111] Q. Wan, Z.T. Song, S.L. Feng, T.H. Wang, Single-crystalline tin-doped indium oxide whiskers: synthesis and characterization, Appl. Phys. Lett. 85 (2004) 4759.
[112] P. Nguyen, H.T. Ng, J. Kong, et al., Epitaxial directional growth of indium-doped tin oxide nanowire arrays, Nano Lett. 3 (2003) 925.
[113] P.D. Yang, The chemistry and physics of semiconductor nanowires, MRS Bull. 30 (2005) 85.
[114] S. Han, C. Li, Z.Q. Liu, et al., Transition metal oxide core–shell nanowires: generic synthesis and transport studies, Nano Lett. 4 (2004) 1241.
[115] J.S. Jie, G.Z. Wang, X.H. Han, J.G. Hou, Synthesis and characterization of ZnO: In nanowires with superlattice structure, J. Phys. Chem. B 108 (2004) 17027.
[116] L.J. Lauhon, M.S. Gudiksen, C.L. Wang, C.M. Lieber, Epitaxial core–shell and core–multi shell nanowire heterostructures, Nature 420 (2002) 57.
[117] W. Lu, J. Xiang, B.P. Timko, Y. Wu, C.M. Lieber, One-dimensional hole gas in germanium/silicon nanowire heterostructures, Proc. Natl. Acad. Sci. U.S.A. 102 (2005) 10046.
[118] F. Qian, S. Gradecak, Y. Li, C.Y. Wen, C.M. Lieber, Core/multishell nanowire heterostructures as multicolor, high-efficiency light-emitting diodes, Nano Lett. 5 (2005) 2287.
[119] H.F. Zhang, C.M. Wang, L.S. Wang, Helical crystalline $SiC/SiO_2$ core–shell nanowires, Nano Lett. 2 (2002) 941.
[120] Y.H. Wong, Q. Li, Study of the crystallinity of ZnO in the Zn/ZnO nanocable heterostructures, J. Mater. Chem. 14 (2004) 1413.

[121] J. Hwang, B.D. Min, J.S. Lee, et al., $Al_2O_3$ nanotubes fabricated by wet etching of ZnO/$Al_2O_3$ core/shell nanofibers, Adv. Mater. 16 (2004) 422.
[122] K.W. Chang, J.J. Wu, Formation of well-aligned $ZnGa_2O_4$ nanowires from $Ga_2O_3$/ZnO core–shell nanowires via a $Ga_2O_3$/$ZnGa_2O_4$ epitaxial relationship, J. Phys. Chem. B 109 (2005) 13572.
[123] J. Xu, X.L. Li, J.F. Liu, X. Wang, Q. Peng, Y.D. Li, Solution route to inorganic nanobelt-conducting organic polymer core–shell nanocomposites, J. Polym. Sci. Part A Polym. Chem. 43 (2005) 2892.
[124] C.W. Lai, J.Y. Dai, X.Y. Zhang, et al., In situ synthesis and phase transformation of $In_2O_3$/Sb core–shell nanostructures, J. Cryst. Growth 282 (2005) 383.
[125] D.H. Zhang, Z.Q. Liu, S. Han, et al., Magnetite ($Fe_3O_4$) core–shell nanowires: synthesis and magnetoresistance, Nano Lett. 4 (2004) 2151.
[126] E.S. Jang, J.Y. Bae, J. Yoo, et al., Quantum confinement effect in ZnO/$Mg_{0.2}Zn_{0.8}O$ multishell nanorod heterostructures, Appl. Phys. Lett. 88 (2006) 023102.
[127] M.S. Gudiksen, L.J. Lauhon, J. Wang, D.C. Smith, C.M. Lieber, Growth of nanowire superlattice structures for nanoscale photonics and electronics, Nature 415 (2002) 617.
[128] Y.Y. Wu, R. Fan, P.D. Yang, Block-by-block growth of single-crystalline Si/SiGe superlattice nanowires, Nano Lett. 2 (2002) 83.
[129] M.T. Bjork, B.J. Ohlsson, T. Sass, et al., One-dimensional heterostructures in semiconductor nanowhiskers, Appl. Phys. Lett. 80 (2002) 1058.
[130] C.W. Na, S.Y. Bae, J. Park, Short-period superlattice structure of Sn-doped $In_2O_3$(ZnO)(4) and $In_2O_3$(ZnO)(5) nanowires, J. Phys. Chem. B 109 (2005) 12785.
[131] P.M. Gao, Y. Ding, W.J. Mai, W.L. Hughes, C.S. Lao, Z.L. Wang, Conversion of zinc oxide nanobelts into superlattice-structured nanohelices, Science 309 (2005) 1700.
[132] Z.Y. Fan, D.W. Wang, P.C. Chang, W.Y. Tseng, J.G. Lu, ZnO nanowire field-effect transistor and oxygen sensing property, Appl. Phys. Lett. 85 (2004) 5923.
[133] P.C. Chang, Z.Y. Fan, J.G. Lu, Appl. Phys. Lett. (2006), submitted for publication.
[134] X.D. Wang, Y. Ding, C.J. Summers, Z.L. Wang, Large-scale synthesis of six-nanometer-wide ZnO nanobelts, J. Phys. Chem. B 108 (2004) 8773.
[135] Y. Gu, I.L. Kuskovsky, M. Yin, S. O'Brien, G.F. Neumark, Quantum confinement in ZnO nanorods, Appl. Phys. Lett. 85 (2004) 3833.
[136] J.S. Jeong, J.Y. Lee, C.J. Lee, S.J. An, G.C. Yi, Synthesis and characterization of high-quality $In_2O_3$ nanobelts via catalyst-free growth using a simple physical vapor deposition at low temperature, Chem. Phys. Lett. 384 (2004) 246.
[137] C. Li, D.H. Zhang, S. Han, X.L. Liu, T. Tang, C.W. Zhou, Diameter-controlled growth of single-crystalline $In_2O_3$ nanowires and their electronic properties, Adv. Mater. 15 (2003) 143.
[138] X.C. Wu, J.M. Hong, Z.J. Han, Y.R. Tao, Fabrication and photoluminescence characteristics of single crystalline $In_2O_3$ nanowires, Chem. Phys. Lett. 373 (2003) 28.
[139] M.J. Zheng, L.D. Zhang, G.H. Li, X.Y. Zhang, X.F. Wang, Ordered indium-oxide nanowire arrays and their photoluminescence properties, Appl. Phys. Lett. 79 (2001) 839.
[140] M.J. Zheng, L.D. Zhang, X.Y. Zhang, J. Zhang, G.H. Li, Fabrication and optical absorption of ordered indium oxide nanowire arrays embedded in anodic alumina membranes, Chem. Phys. Lett. 334 (2001) 298.
[141] F. Liu, M. Bao, K.L. Wang, C. Li, B. Lei, C. Zhou, One-dimensional transport of $In_2O_3$ nanowires, Appl. Phys. Lett. 86 (2005) 213101.
[142] M. Ogita, N. Saika, Y. Nakanishi, Y. Hatanaka, $Ga_2O_3$ thin films for high-temperature gas sensors, Appl. Surf. Sci. 142 (1999) 188.
[143] X.C. Wu, W.H. Song, W.D. Huang, et al., Crystalline gallium oxide nanowires: intensive blue light emitters, Chem. Phys. Lett. 328 (2000) 5.
[144] G.S. Park, W.B. Choi, J.M. Kim, Y.C. Choi, Y.H. Lee, C.B. Lim, Structural investigation of gallium oxide (beta-$Ga_2O_3$) nanowires grown by arc-discharge, J. Cryst. Growth 220 (2000) 494.
[145] G. Gundiah, A. Govindaraj, C.N.R. Rao, Nanowires, nanobelts and related nanostructures of $Ga_2O_3$, Chem. Phys. Lett. 351 (2002) 189.
[146] Z.R. Dai, Z.W. Pan, Z.L. Wang, Gallium oxide nanoribbons and nanosheets, J. Phys. Chem. B 106 (2002) 902.
[147] M.F. Yu, M.Z. Atashbar, X.L. Chen, Mechanical and electrical characterization of beta-$Ga_2O_3$ nanostructures for sensing applications, IEEE Sens. J. 5 (2005) 20.
[148] E. Nogales, B. Mendez, J. Piqueras, Cathodoluminescence from beta-$Ga_2O_3$ nanowires, Appl. Phys. Lett. 86 (2005) 113112.

[149] D.P. Yu, J.L. Bubendorff, J.F. Zhou, Y. Leprince-Wang, M. Troyon, Localized cathodoluminescence investigation on single $Ga_2O_3$ nanoribbon/nanowire, Solid State Commun. 124 (2002) 417.
[150] B. Cheng, J.M. Russell, W.S. Shi, L. Zhang, E.T. Samulski, Large-scale, solution-phase growth of single-crystalline $SnO_2$ nanorods, J. Am. Chem. Soc. 126 (2004) 5972.
[151] D. Calestani, M. Zha, A. Zappettini, et al., Structural and optical study of $SnO_2$ nanobelts and nanowires, Mater. Sci. Eng. C Biomimetic Supramol. Syst. 25 (2005) 625.
[152] W.T. Dong, C.S. Zhu, Use of ethylene oxide in the sol–gel synthesis of alpha-$Fe_2O_3$ nanoparticles from Fe(III) salts, J. Mater. Chem. 12 (2002) 1676.
[153] P. Li, D.E. Miser, S. Rabiei, R.T. Yadav, M.R. Hajaligol, The removal of carbon monoxide by iron oxide nanoparticles, Appl. Catal. B Environ. 43 (2003) 151.
[154] X.G. Wen, S.H. Wang, Y. Ding, Z.L. Wang, S.H. Yang, Controlled growth of large-area, uniform, vertically aligned arrays of alpha-$Fe_2O_3$ nanobelts and nanowires, J. Phys. Chem. B 109 (2005) 215.
[155] Y.Y. Fu, J. Chen, H. Zhang, Synthesis of $Fe_2O_3$ nanowires by oxidation of iron, Chem. Phys. Lett. 350 (2001) 491.
[156] H.Z. Wang, X.T. Zhang, B. Liu, et al., Synthesis and characterization of single crystal alpha-$Fe_2O_3$ nanobelts, Chem. Lett. 34 (2005) 184.
[157] C.J. Jia, L.D. Sun, Z.G. Yan, et al., Iron oxide nanotubes—single-crystalline iron oxide nanotubes, Angewandte Chem. Int. Ed. 44 (2005) 4328.
[158] J. Wang, Q.W. Chen, C. Zeng, B.Y. Hou, Magnetic-field-induced growth of single-crystalline $Fe_3O_4$ nanowires, Adv. Mater. 16 (2004) 137.
[159] G.B. Ji, S.L. Tang, S.K. Ren, F.M. Zhang, B.X. Gu, Y.W. Du, Simplified synthesis of single-crystalline magnetic $CoFe_2O_4$ nanorods by a surfactant-assisted hydrothermal process, J. Cryst. Growth 270 (2004) 156.
[160] J. Wang, Q.W. Chen, B.Y. Hou, Z.M. Peng, Synthesis and magnetic properties of single-crystals of $MnFe_2O_4$ nanorods, Eur. J. Inorg. Chem. (2004) 1165.
[161] D.E. Zhang, X.J. Zhang, X.M. Ni, H.G. Zheng, D.D. Yang, Synthesis and characterization of $NiFe_2O_4$ magnetic nanorods via a PEG-assisted route, J. Magn. Magn. Mater. 292 (2005) 79.
[162] J.B. Reitz, E.I. Solomon, Propylene oxidation on copper oxide surfaces: electronic and geometric contributions to reactivity and selectivity, J. Am. Chem. Soc. 120 (1998) 11467.
[163] J. Chen, N.Y. Huang, S.Z. Deng, et al., Effects of light illumination on field emission from CuO nanobelt arrays, Appl. Phys. Lett. 86 (2005) 151107.
[164] X.G. Wen, Y.T. Xie, C.L. Choi, K.C. Wan, X.Y. Li, S.H. Yang, Copper-based nanowire materials: templated syntheses, characterizations, and applications, Langmuir 21 (2005) 4729.
[165] T.J. Coutts, D.L. Young, X. Li, W.P. Mulligan, X. Wu, Search for improved transparent conducting oxides: a fundamental investigation of CdO, $Cd_2SnO_4$, and $Zn_2SnO_4$, J. Vacuum Sci. Technol. A Vacuum Surf. Films 18 (2000) 2646.
[166] G.L. Li, G.H. Wang, J.M. Hong, Synthesis and characterization of rutile $TiO_2$ nanowhiskers, J. Mater. Res. 14 (1999) 3346.
[167] Z. Miao, D.S. Xu, J.H. Ouyang, G.L. Guo, X.S. Zhao, Y.Q. Tang, Electrochemically induced sol–gel preparation of single-crystalline $TiO_2$ nanowires, Nano Lett. 2 (2002) 717.
[168] L. Miao, S. Tanemura, S. Toh, K. Kaneko, M. Tanemura, Fabrication, characterization and Raman study of anatase $TiO_2$ nanorods by a heating-sol–gel template process, J. Cryst. Growth 264 (2004) 246.
[169] D. Li, Y.N. Xia, Fabrication of titania nanofibers by electrospinning, Nano Lett. 3 (2003) 555.
[170] L. Kavan, M. Kalbac, M. Zukalova, et al., Lithium storage in nanostructured $TiO_2$ made by hydrothermal growth, Chem. Mater. 16 (2004) 477.
[171] B.M. Wen, C.Y. Liu, Y. Liu, Bamboo-shaped Ag-doped $TiO_2$ nanowires with heterojunctions, Inorg. Chem. 44 (2005) 6503.
[172] J.M. Wu, H.C. Shih, W.T. Wu, Formation and photoluminescence of single-crystalline rutile $TiO_2$ nanowires synthesized by thermal evaporation, Nanotechnology 17 (2006) 105.
[173] A.R. Armstrong, G. Armstrong, J. Canales, R. Garcia, P.G. Bruce, Lithium-ion intercalation into $TiO_2$-B nanowires, Adv. Mater. 17 (2005) 862.
[174] C.J. Patrissi, C.R. Martin, Sol–gel-based template synthesis and Li-insertion rate performance of nanostructured vanadium pentoxide, J. Electrochem. Soc. 146 (1999) 3176.
[175] J. Muster, G.T. Kim, V. Krstic, et al., Electrical transport through individual vanadium pentoxide nanowires, Adv. Mater. 12 (2000) 420.
[176] K. Takahashi, S.J. Limmer, Y. Wang, G.Z. Cao, Synthesis and electrochemical properties of single-crystal $V_2O_5$ nanorod arrays by template-based electrodeposition, J. Phys. Chem. B 108 (2004) 9795.

[177] S. Webster, R. Czerw, R. Nesper, et al., Optical properties of vanadium oxide nanotubes, J. Nanosci. Nanotechnol. 4 (2004) 260.
[178] Y. Wang, K. Takahashi, H.M. Shang, G.Z. Cao, Synthesis and electrochemical properties of vanadium pentoxide nanotube arrays, J. Phys. Chem. B 109 (2005) 3085.
[179] K. Takahashi, Y. Wang, K. Lee, G. Cao, Fabrication and Li+-intercalation properties of $V_2O_5$–$TiO_2$ composite nanorod arrays, Appl. Phys. A Mater. Sci. Process. 82 (2006) 27.
[180] R. Martel, T. Schmidt, H.R. Shea, T. Hertel, P. Avouris, Single- and multi-wall carbon nanotube field-effect transistors, Appl. Phys. Lett. 73 (1998) 2447.
[181] F.M. Hossain, J. Nishii, S. Takagi, et al., Modeling of grain boundary barrier modulation in ZnO invisible thin film transistors, Phys. E Low-Dimensional Syst. Nanostruct. 21 (2004) 911.
[182] W.I. Park, J.S. Kim, G.C. Yi, M.H. Bae, H.J. Lee, Fabrication and electrical characteristics of high-performance ZnO nanorod field-effect transistors, Appl. Phys. Lett. 85 (2004) 5052.
[183] P. Nguyen, H.T. Ng, T. Yamada, et al., Direct integration of metal oxide nanowire in vertical field-effect transistor, Nano Lett. 4 (2004) 651.
[184] T. Marinov, A. Buldum, C.B. Clemons, K.L. Kreider, G.W. Young, S.I. Hariharan, Field emission from coated nanowires, J. Appl. Phys. 98 (2005) 044314.
[185] C.J. Lee, T.J. Lee, S.C. Lyu, Y. Zhang, H. Ruh, H.J. Lee, Field emission from well-aligned zinc oxide nanowires grown at low temperature, Appl. Phys. Lett. 81 (2002) 3648.
[186] R.S. Chen, Y.S. Huang, Y.M. Liang, C.S. Hsieh, D.S. Tsai, K.K. Tiong, Field emission from vertically aligned conductive $IrO_2$ nanorods, Appl. Phys. Lett. 84 (2004) 1552.
[187] C.S. Hsieh, G. Wang, D.S. Tsai, R.S. Chen, Y.S. Huang, Field emission characteristics of ruthenium dioxide nanorods, Nanotechnology 16 (2005) 1885.
[188] H.S. Jang, D.H. Kim, H.R. Lee, S.Y. Lee, Field emission from cone-like single crystalline indium tin oxide nanorods, Mater. Lett. 59 (2005) 1526.
[189] S.Q. Li, Y.X. Liang, T.H. Wang, Electric-field-aligned vertical growth and field emission properties of $In_2O_3$ nanowires, Appl. Phys. Lett. 87 (2005) 143104.
[190] J.G. Liu, Z.J. Zhang, Y. Zhao, X. Su, S. Liu, E.G. Wang, Tuning the field-emission properties of tungsten oxide nanorods, Small 1 (2005) 310.
[191] J.M. Wu, H.C. Shih, W.T. Wu, Electron field emission from single crystalline $TiO_2$ nanowires prepared by thermal evaporation, Chem. Phys. Lett. 413 (2005) 490.
[192] L. Liao, J.C. Li, D.F. Wang, et al., Field emission property improvement of ZnO nanowires coated with amorphous carbon and carbon nitride films, Nanotechnology 16 (2005) 985.
[193] C.X. Xu, X.W. Sun, B.J. Chen, Field emission from gallium-doped zinc oxide nanofiber array, Appl. Phys. Lett. 84 (2004) 1540.
[194] Q. Zhao, X.Y. Xu, X.F. Song, et al., Enhanced field emission from ZnO nanorods via thermal annealing in oxygen, Appl. Phys. Lett. 88 (2006) 033102.
[195] W.I. Park, J.S. Kim, G.C. Yi, H.J. Lee, ZnO nanorod logic circuits, Adv. Mater. 17 (2005) 1393.
[196] M. Law, D.J. Sirbuly, J.C. Johnson, J. Goldberger, R.J. Saykally, P.D. Yang, Nanoribbon waveguides for sub-wavelength photonics integration, Science 305 (2004) 1269.
[197] J.C. Johnson, H.Q. Yan, P.D. Yang, R.J. Saykally, Optical cavity effects in ZnO nanowire lasers and waveguides, J. Phys. Chem. B 107 (2003) 8816.
[198] D.K. Hwang, S.H. Kang, J.H. Lim, et al., *p*-ZnO/*n*-GaN heterostructure ZnO light-emitting diodes, Appl. Phys. Lett. 86 (2005) 222101.
[199] S.J. Jiao, Z.Z. Zhang, Y.M. Lu, et al., ZnO *p*–*n* junction light-emitting diodes fabricated on sapphire substrates, Appl. Phys. Lett. 88 (2006) 031911.
[200] R. Konenkamp, R.C. Word, C. Schlegel, Vertical nanowire light-emitting diode, Appl. Phys. Lett. 85 (2004) 6004.
[201] H. Kind, H.Q. Yan, B. Messer, M. Law, P.D. Yang, Nanowire ultraviolet photodetectors and optical switches, Adv. Mater. 14 (2002) 158.
[202] Z.Y. Fan, P.C. Chang, J.G. Lu, et al., Photoluminescence and polarized photodetection of single ZnO nanowires, Appl. Phys. Lett. 85 (2004) 6128.
[203] D. Zhang, C. Li, S. Han, et al., Ultraviolet photodetection properties of indium oxide nanowires, Appl. Phys. A Mater. Sci. Process. 77 (2003) 163.
[204] Y.W. Heo, L.C. Tien, D.P. Norton, et al., Electrical transport properties of single ZnO nanorods, Appl. Phys. Lett. 85 (2004) 2002.

[205] K. Keem, H. Kim, G.T. Kim, et al., Photocurrent in ZnO nanowires grown from Au electrodes, Appl. Phys. Lett. 84 (2004) 4376.
[206] K.P. Jayadevan, T.Y. Tseng, One-dimensional semiconductor nanostructures as absorber layers in solar cells, J. Nanosci. Nanotechnol. 5 (2005) 1768.
[207] M. Law, L.E. Greene, J.C. Johnson, R. Saykally, P.D. Yang, Nanowire dye-sensitized solar cells, Nat. Mater. 4 (2005) 455.
[208] J.T. Jiu, F.M. Wang, S. Isoda, M. Adachi, Highly efficient dye-sensitized solar cells based on single crystalline $TiO_2$ nanorod film, Chem. Lett. 34 (2005) 1506.
[209] S. Anandan, X.G. Wen, S.H. Yang, Room temperature growth of CuO nanorod arrays on copper and their application as a cathode in dye-sensitized solar cells, Mater. Chem. Phys. 93 (2005) 35.
[210] P.J. Michalski, N. Sai, E.J. Mele, Continuum theory for nanotube piezoelectricity, Phys. Rev. Lett. 95 (2005) 116803.
[211] Z.L. Wang, Z.R. Dai, R.P. Gao, J.L. Gole, Measuring the Young's modulus of solid nanowires by in situ TEM, J. Electron. Microsc. 51 (2002) S79.
[212] Z.L. Wang, New developments in transmission electron microscopy for nanotechnology, Adv. Mater. 15 (2003) 1497.
[213] M.H. Zhao, Z.L. Wang, S.X. Mao, Piezoelectric characterization of individual zinc oxide nanobelt probed by piezoresponse force microscope, Nano Lett. 4 (2004) 587.
[214] Z.L. Wang, Properties of nanobelts and nanotubes measured by in situ TEM, Microsc. Microanal. 10 (2004) 158.
[215] J.H. Song, X.D. Wang, E. Riedo, Z.L. Wang, Elastic property of vertically aligned nanowires, Nano Lett. 5 (2005) 1954.
[216] Z.L. Wang, R.P. Gao, Z.W. Pan, Z.R. Dai, Nano-scale mechanics of nanotubes, nanowires, and nanobelts, Adv. Eng. Mater. 3 (2001) 657.
[217] D.A. Dikin, X. Chen, W. Ding, G. Wagner, R.S. Ruoff, Resonance vibration of amorphous $SiO_2$ nanowires driven by mechanical or electrical field excitation, J. Appl. Phys. 93 (2003) 226.
[218] T. Ikuno, S. Honda, T. Yasuda, et al., Thermally driven nanomechanical deflection of hybrid nanowires, Appl. Phys. Lett. 87 (2005) 213104.
[219] G. Suyal, E. Colla, R. Gysel, M. Cantoni, N. Setter, Piezoelectric response and polarization switching in small anisotropic perovskite particles, Nano Lett. 4 (2004) 1339.
[220] X.Y. Zhang, X. Zhao, C.W. Lai, J. Wang, X.G. Tang, J.Y. Dai, Synthesis and piezoresponse of highly ordered $Pb(Zr_{0.53}Ti_{0.47})O_3$ nanowire arrays, Appl. Phys. Lett. 85 (2004) 4190.
[221] S.T. Shishiyanu, T.S. Shishiyanu, O.I. Lupan, Sensing characteristics of tin-doped ZnO thin films as $NO_2$ gas sensor, Sens. Actuators B Chem. 107 (2005) 379.
[222] R. Ramamoorthy, P.K. Dutta, S.A. Akbar, Oxygen sensors: materials, methods, designs and applications, J. Mater. Sci. 38 (2003) 4271.
[223] Z.Y. Fan, J.G. Lu, Gate-refreshable nanowire chemical sensors, Appl. Phys. Lett. 86 (2005) 123510.
[224] A. Kolmakov, M. Moskovits, Chemical sensing and catalysis by one-dimensional metal–oxide nanostructures, Annu. Rev. Mater. Res. 34 (2004) 151.
[225] A. Kolmakov, Y.X. Zhang, G.S. Cheng, M. Moskovits, Detection of CO and $O_2$ using tin oxide nanowire sensors, Adv. Mater. 15 (2003) 997.
[226] C. Baratto, E. Comini, G. Faglia, G. Sberveglieri, M. Zha, A. Zappettini, Metal oxide nanocrystals for gas sensing, Sens. Actuators B Chem. 109 (2005) 2.
[227] H. Nanto, T. Minami, S. Takata, Zinc-oxide thin-film ammonia gas sensors with high-sensitivity and excellent selectivity, J. Appl. Phys. 60 (1986) 482.
[228] G. Faglia, P. Nelli, G. Sberveglieri, Frequency effect on highly sensitive $NO_2$ sensors based on Rgto $SNO_2$(al), Thin-Films Sens. Actuators B Chem. 19 (1994) 497.
[229] A. Heilig, N. Barsan, U. Weimar, M. Schweizer-Berberich, J.W. Gardner, W. Gopel, Gas identification by modulating temperatures of $SnO_2$-based thick film sensors, Sens. Actuators B Chem. 43 (1997) 45.
[230] Q.F. Pengfei, O. Vermesh, M. Grecu, et al., Toward large arrays of multiplex functionalized carbon nanotube sensors for highly sensitive and selective molecular detection, Nano Lett. 3 (2003) 347.
[231] Y. Zhang, A. Kolmakov, S. Chretien, H. Metiu, M. Moskovits, Control of catalytic reactions at the surface of a metal oxide nanowire by manipulating electron density inside it, Nano Lett. 4 (2004) 403.
[232] A.M. Azad, S.A. Akbar, S.G. Mhaisalkar, L.D. Birkefeld, K.S. Goto, Solid-state gas sensors—a review, J. Electrochem. Soc. 139 (1992) 3690.
[233] G. Eranna, B.C. Joshi, D.P. Runthala, R.P. Gupta, Oxide materials for development of integrated gas sensors—a comprehensive review, Crit. Rev. Solid State Mater. Sci. 29 (2004) 111.

[234] B.S. Kang, Y.W. Heo, L.C. Tien, et al., Hydrogen and ozone gas sensing using multiple ZnO nanorods, Appl. Phys. A Mater. Sci. Process. 80 (2005) 1029.
[235] Z.Y. Fan, J.G. Lu, Chemical sensing with ZnO nanowire field-effect transistor, IEEE Trans. Nano., in press (2006).
[236] Y.S. Kim, S.C. Ha, K. Kim, et al., Room-temperature semiconductor gas sensor based on nonstoichiometric tungsten oxide nanorod film, Appl. Phys. Lett. 86 (2005) 213105.
[237] L.C. Tien, P.W. Sadik, D.P. Norton, et al., Hydrogen sensing at room temperature with Pt-coated ZnO thin films and nanorods, Appl. Phys. Lett. 87 (2005) 222106.
[238] H.T. Wang, B.S. Kang, F. Ren, et al., Hydrogen-selective sensing at room temperature with ZnO nanorods, Appl. Phys. Lett. 86 (2005) 243503.
[239] J.Q. Xu, Y.P. Chen, Y.D. Li, J.N. Shen, Gas sensing properties of ZnO nanorods prepared by hydrothermal method, J. Mater. Sci. 40 (2005) 2919.
[240] C.H. Wang, X.F. Chu, M.W. Wu, Detection of $H_2S$ down to ppb levels at room temperature using sensors based on ZnO nanorods, Sens. Actuators B Chem. 113 (2006) 320.
[241] Q. Wan, Q.H. Li, Y.J. Chen, et al., Fabrication and ethanol sensing characteristics of ZnO nanowire gas sensors, Appl. Phys. Lett. 84 (2004) 3654.
[242] E. Comini, G. Faglia, G. Sberveglieri, D. Calestani, L. Zanotti, M. Zha, Tin oxide nanobelts electrical and sensing properties, Sens. Actuators B Chem. 111 (2005) 2.
[243] S.V. Kalinin, J. Shin, S. Jesse, et al., Electronic transport imaging in a multiwire $SnO_2$ chemical field-effect transistor device, J. Appl. Phys. 98 (2005) 044503.
[244] Z. Ying, Q. Wan, Z.T. Song, S.L. Feng, $SnO_2$ nanowhiskers and their ethanol sensing characteristics, Nanotechnology 15 (2004) 1682.
[245] Q. Wan, T.H. Wang, Single-crystalline Sb-doped $SnO_2$ nanowires: synthesis and gas sensor application, Chem. Commun. (2005) 3841.
[246] A. Kolmakov, D.O. Klenov, Y. Lilach, S. Stemmer, M. Moskovits, Enhanced gas sensing by individual $SnO_2$ nanowires and nanobelts functionalized with Pd catalyst particles, Nano Lett. 5 (2005) 667.
[247] C. Yu, Q. Hao, S. Saha, L. Shi, X.Y. Kong, Z.L. Wang, Integration of metal oxide nanobelts with microsystems for nerve agent detection, Appl. Phys. Lett. 86 (2005) 063101.
[248] X.F. Chu, C.H. Wang, D.L. Jiang, C.M. Zheng, Ethanol sensor based on indium oxide nanowires prepared by carbothermal reduction reaction, Chem. Phys. Lett. 399 (2004) 461.
[249] C. Li, D.H. Zhang, X.L. Liu, et al., $In_2O_3$ nanowires as chemical sensors, Appl. Phys. Lett. 82 (2003) 1613.
[250] D.H. Zhang, Z.Q. Liu, C. Li, et al., Detection of $NO_2$ down to ppb levels using individual and multiple $In_2O_3$ nanowire devices, Nano Lett. 4 (2004) 1919.
[251] J.F. Liu, X. Wang, Q. Peng, Y.D. Li, Vanadium pentoxide nanobelts: highly selective and stable ethanol sensor materials, Adv. Mater. 17 (2005) 764.
[252] I. Raible, M. Burghard, U. Schlecht, A. Yasuda, T. Vossmeyer, $V_2O_5$ nanofibres: novel gas sensors with extremely high sensitivity and selectivity to amines, Sens. Actuators B Chem. 106 (2005) 730.
[253] K.M. Sawicka, A.K. Prasad, P.I. Gouma, Metal oxide nanowires for use in chemical sensing applications, Sens. Lett. 3 (2005) 31.
[254] J. Polleux, A. Gurlo, N. Barsan, U. Weimar, M. Antonietti, M. Niederberger, Template-free synthesis and assembly of single-crystalline tungsten oxide nanowires and their gas-sensing properties, Angewandte Chem. Int. Ed. 45 (2006) 261.
[255] Q. Wan, Q.H. Li, Y.J. Chen, T.H. Wang, X.L. He, X.G. Gao, J.P. Li, Positive temperature coefficient resistance and humidity sensing properties of Cd-doped ZnO nanowires, Appl. Phys. Lett. 84 (2004) 3085.